École Polytechnique Fédérale de Lausanne

MASTER THESIS

Powder Characterisation of Zinc-Modified Synthetic Calcium Silicate Hydrate (C-S-H)

Autor: Arnau Sola Blasco

Responsible: Anna Morales Melgares

Supervisor: Prof. Paul Bowen

June 3, 2022

Abstract

Despite being one of the most abundant materials in the world, several aspects of C-S-H still remain unknown. It has been shown that minor additions of zinc enhance the early age strength of the cement's clinker as it increases C-S-H reactivity, but the mechanisms behind this are still unclear. As C-S-H is the main hydration product of cement, understanding the effect of zinc on it's growth can help improve cement's properties and thus lower its CO_2 emissions by partially substituting it with SCMs.

In this project, high Ca:Si ratio (>1.5) C-S-H and Zn-modified C-S-H have been successfully synthesized by a dropwise precipitation method. Samples were preliminary characterised through XRD, which confirmed that zinc was incorporated into the structure of C-S-H and no new phases were formed. TGA quantified the bound water, carbonation and portlandite losses. It also showed that portlandite formation did not have a significant impact in the corrected Ca:Si ratio. TEM micrographs showed the nanofoil morphology of both C-S-H and Zn-modified C-S-H.

Particle size distributions (PSD) were studied using laser diffraction., concluding that C-S-H was agglomerating into particles that are 1-20 µm. PSD frequency plots also showed the formation of two main agglomerates families of 4.9 and 6.6 µm, regardless of the amount of zinc. SSA values, obtained through N_2 adsorption experiment and using the BET model, oscillated between 133 and 325 m^2/g. When both values from PSD and SSA were used, an agglomeration factor F_{AG} could be calculated. It ranged from 110 to 171, which concludes that the C-S-H is a very heavy agglomerated powder.

Also, zeta potential results indicated that positive Na^+ and Ca^{+2} ions adsorbed from the dispersion media onto the C-S-H surface, with a preference for the latter when both were competing. Also, when supernatant was used as the dispersion medium, zeta potential values decreased for Zn-modified C-S-H. This supports the current Zn-modified C-S-H atomistic structure theory, which points to zinc substituting silicon and calcium atoms in C-S-H surface.

EPFL

Outline

EPFL

EPFL

List of Figures

EPFL

EPFL

EPFL

List of Tables

EPFL

List of Abbreviations

C₃S　　　　　Alite $3CaO \cdot SiO_2$

C₂S　　　　　Belite $2CaO \cdot SiO_2$

C₃A　　　　　Tricalcium aluminate $3CaO \cdot Al_2O_3$

C₄AF　　　　Ferrite $Ca_2Al_xFe_{2-x}O$

C-S-H　　　Calcium silicate hydrate $CaO \cdot SiO_2 \cdot H_2O$

DTG　　　　　Differential or derivative thermogravimetry

LD　　　　　　Laser diffraction

LMC　　　　　Laboratory of Construction Materials

NMR　　　　　Nuclear magnetic resonance

OM　　　　　　Optical microscopy

PSD　　　　　Particle size distribution

PTG　　　　　Powder Technology Group

SCM　　　　　Supplementary cementitious material

SEM　　　　　Scanning electron microscopy

SSA　　　　　Specific surface area

TEM　　　　　Transmission electron microscopy

TGA　　　　　Thermogravimetric analysis

XRD　　　　　X-ray diffraction

EPFL

1. General introduction

1.1 Context

This project has been developed within the Powder Technology Group (PTG), which is part of the Laboratory of Construction Materials (LMC) at EPFL. PTG joined the LMC in March 2018 after being part of the Powder Technology Laboratory (LTP) at EPFL since 1988. PTG is concerned with the research, development, and processing of inorganic particles at a nano and micro scale.

The group has as its goals the understanding at a fundamental level the steps comprised in materials fabrication, from the synthesis of the powders until the final product, with a view to improving materials properties of technological importance. The activities of PTG are carried out in the form of projects translating fundamental knowledge of growth and particle interaction mechanisms into the many different areas of application. The current focus of research is on calcium silicate hydrates and calcium phosphates for both construction and biomedical applications.

This master thesis has been carried out within the "Minor Elements Project", which aims to offer a full picture of C-S-H thermodynamics, kinetics, growth mechanisms and atomic structure when minor elements are added, with a special focus on zinc. Overall, the Minor Elements Project is subdivided into three doctoral theses: the atomistic modelling of synthetic C-S-H with minor elements (Ziga Casar), the analysis of real cementitious systems with minor elements (Andrea Teixeira) and the synthesis and analysis of synthetic C-S-H with minor elements (Anna Morales).

More precisely, this master thesis is mainly under the umbrella of the last doctoral thesis mentioned and aims to expand its study by further analysing the C-S-H behaviour in presence of zinc.

EPFL

1.2 Objectives of the project

It has been shown that zinc can enhance the mechanical strength of the clinker during the hydration of the anhydrous cement blend. [[1], [2]] However, cement is composed by multiple phases and the kinetics and thermodynamics of the hydration reaction are extremely complex. Thus, it is required to study the overall system in smaller parts, i.e., reduce the number of degrees of freedom to obtain more accurate conclusions.

The aim of this project is to study only the C-S-H, which is the main binder material and the main contributor of the early-age strength of cement, [3] with different zinc additions at a Ca:Si ratios similar to those in real systems (i.e. 1.7-2). Consequently, the main goal of this thesis is to characterise the Zn-modified C-S-H to elucidate which is the effect of the zinc on general C-S-H properties.

Several more concrete objectives arise from this main goal.

- C-S-H and Zn-modified C-S-H synthesis at high Ca:Si ratios (>1.5).

- Characterisation through X-ray diffraction and thermogravimetric analysis to ensure that the C-S-H synthesized is mostly single-phase.

- C-S-H characterisation through optical and transmission electron microscopy.

- Particle Size Distribution study and observation of the possible variations from C-S-H to Zn-modified C-S-H through laser diffraction.

- Measurement of a specific surface area for C-S-H with and without zinc through nitrogen adsorption.

- Results comparison with those of atomistic simulations made within PTG.

- Surface characterisation of C-S-H and Zn-modified C-S-H through zeta potential measurements.

EPFL

2. State of the art

2.1 Cement, SCMs and minor elements

2.1.1 Portland Cements

Concrete is the most widely produced man-made material in the world, and the second most consumed resource only after water. [4] It is a heterogeneous material composed by aggregates (mainly sand) bonded together with cement paste. The most well-known and widely used cement is Portland cement, which was first invented by Joseph Aspdin in 1824. Because it relies on raw materials that are easily accessible on earth crust such as limestone and clay, Portland cement remains nowadays as the dominant type of cement in the worldwide concrete production. [5] It is produced by mixing the SiO_2 from the clay altogether with the $CaCO_3$ present in the limestone and warming the blend at 1450 ºC, forming what is known as "clinker". Once the clinker is mixed with water, the hydration reaction starts, forming the cement paste. To achieve these high temperatures, a great amount of energy is required and the reaction releases about 0.7 kg of CO_2 per kilogram of cement. Most of these emissions are coming from the breakdown of limestone, which is 80% of the raw material used to produce Portland Cement, [6] and it is often referred to as "chemical" CO_2.

Despite being a material with a relatively low carbon footprint per kg, it is the source of 5-8% of the world's CO_2 emissions due to its massive production. To put this into perspective, if all the cement industry were a country, it would be the third biggest CO_2 emitter in the world behind China and USA. Moreover, the demand for cementitious materials is expected to increase in the following years and, with it, their CO_2-related emissions. [4] Therefore, there is an urgent need for novel solutions which can help mitigate this impact and that are as eco-friendly as accessible, without compromising the mechanical properties of the material.

Portland Cement is a heterogeneous material composed mainly by a mixture of calcium and silicon oxides that, in contact with water, undergo a reaction of hydration. Before the reaction, the anhydrous Portland clinkers are compounded by four main phases: alite, belite, tricalcium aluminate, and ferrite. Alite, the main phase, is an impure C_3S which constitutes more than 50% of the mixture in weight. The second main phase, belite, is an impure C_2S. The last two are tricalcium aluminate (C_3A), and ferrite (C_4AF). [[7], [8]] When water is added into the anhydrous clinker, the hydration reaction starts and while these anhydrous phases begin to dissolve, new oversaturated phases start to precipitate; these are the so-called hydration products. [9]

Between these new phases that precipitate, the most important ones are: Calcium Silicate Hydrate (C-S-H), portlandite, ettringite, calcium carbonate, calcium aluminate monosulfate and hydrogarnets. [[10], [11], [12]] These hydration products are responsible for the cement

EPFL

hardening because they act as binders for the anhydrous grains which are not fully dissolved during hydration. Figure 1 shows a micrograph of a cement sample with several different anhydrous phases and hydration products.
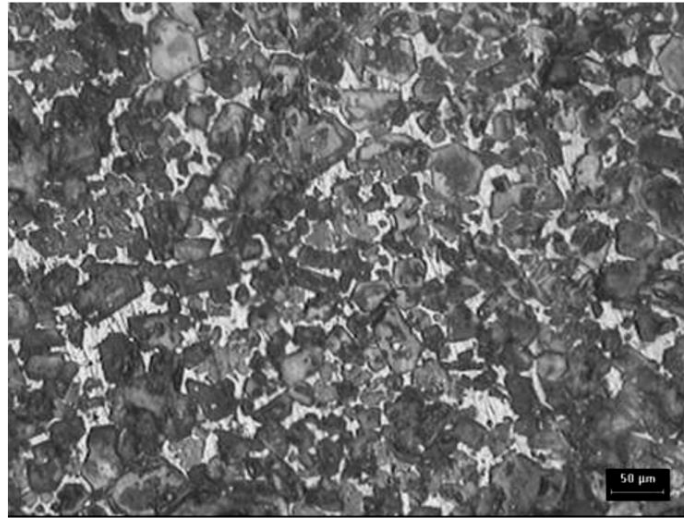
Figure 1: Micrograph of Portland cement. [13]

Looking at the hydration reaction of cement in more detail, Figure 2 shows the typical heat rate evolution curve versus hydration time. Ther are five main stages of hydration: [14] the initial reaction, the induction period, the acceleration period and the deceleration period. After an initial burst, during the induction period the activity is low, which provides time for concrete to be mixed, transported, and placed. Then, during the acceleration period, the silicates hydrate rapidly, reaching what is known as the "maximum rate of heat evolution". From then on, in the following deceleration period, the reaction is no longer chemically controlled but due to diffusion mechanisms. Finally, after 24 hours, the rate of reaction is low, but the reaction still continues. It is relevant to note that, after one day, concrete will typically have only 25% of the design strength. [15]
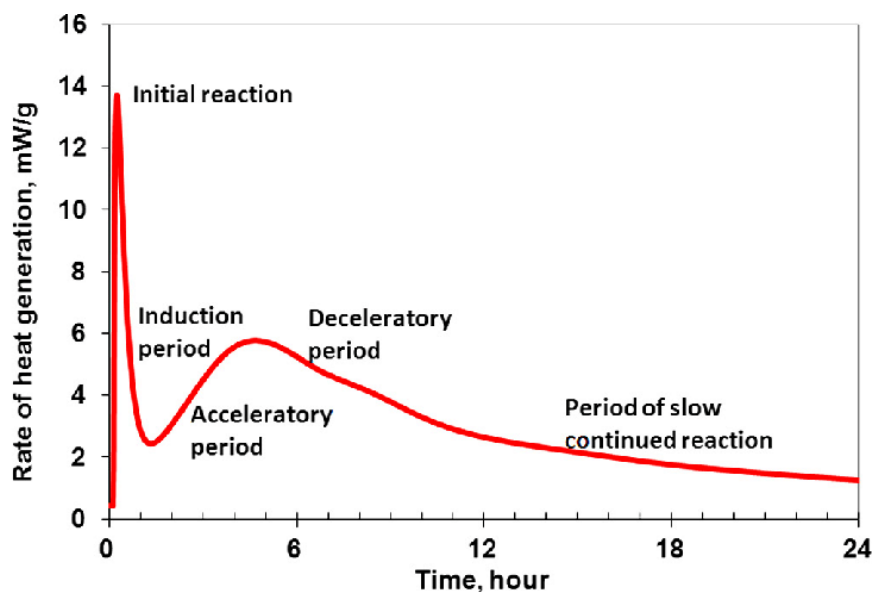
Figure 2: Example of a heat evolution curve for Portland cement. [15]

EPFL

2.1.2 SCMs

As mentioned, the chemical decomposition of the $CaCO_3$ contained in the limestone is the main responsible for the CO_2 emissions, the reaction is as follows: [16]

$$CaCO_3 \rightarrow CaO + CO_2$$
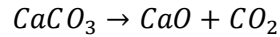
Subsequently, it is the principal focus to address so that these emissions can be mitigated. Amongst all the different solutions studied, the most relevant ones are the supplementary cementitious materials, also known as SCMs. [17]

SCMs are materials that contribute to the properties of cement through hydraulic activity. The main advantage they have over common Portland cement is that their production is more sustainable. Unfortunately, due to their significantly lower properties like reactivity, SCMs can only be added in smaller quantities. Therefore, the usual procedure is to substitute part of the clinker with small amounts of SCMs, so that the CO_2 emissions per kg of cement can be mitigated without compromising the final properties of hardened concrete. [[17], [18], [19], [20]]

The most relevant SCMs are fly ash (FA), which is a waste product from coal fired power production; and granulated blast furnace slag (GBFS), which is by-product of the production of iron and steel. Currently, the average level of substitution worldwide is only about 20%, due to its limited availability. [21] One of the most promising solutions nowadays are calcined clays, which are a major research activity in LMC. [[18], [22], [23]] They would help solve the mentioned problem, as they are suitable materials widely available around the world in virtually unlimited quantities.

It is important to note that the higher reactivity the clinker has, the higher substitution of SCMs can be possible and, therefore, the more sustainable this "composite" or "blended" cement is. For this reason, it is essential to put the focus on improving the properties of the clinker, or more precisely, in its most abundant hydration product: C-S-H.

2.1.3 Minor Elements

As mentioned, SCMs offer a great solution for making the cement more sustainable, but it comes along with a demanding challenge: the need for improving the clinker's physical properties.

To achieve this goal, the addition of minor elements like zinc has been shown to be a suitable option. Even though it has been demonstrated that addition of zinc compounds during mixing can lead to severe retardation of hydration (lowering the early age strength of the blend), [[24], [25]] recent investigation seems to conclude that lowering the concentration of zinc can lead to an opposite effect. This enhancing of the alite's mechanical strength seems to happen during the reaction of hydration. However, understanding such effects is not a trivial task, as the overall reaction scheme is complex due to the high number

EPFL

of phases that dissolve and precipitate at the same time.

Regarding the choice between different minor elements, the work done by *Bazzoni et al.* [1] concludes that the reactivity of the alite grains is increased with smaller uptakes of zinc, while magnesium incorporation produces a different polymorph with very similar reactivity. Moreover, although both magnesium and zinc influence the main peak of hydration, they do it in two different ways. While zinc gives a higher peak, magnesium gives a wider one. These two behaviours appear to be related to the modification of nucleation and growth of C-S-H. In light of the above, cementitious materials with zinc additions seems to be more promising than with magnesium additions.

In this project, it will be studied into further detail the effect of zinc on the physical properties of C-S-H, which controls the main hydration peak of cement. By simplifying the system into its main compound, the aim is to better elucidate the exact effect of zinc on C-S-H properties.

2.2 C-S-H

2.2.1 C-S-H formation

As stated, C-S-H is the main hydration product in cement, composing 50-60% of its volume. Even though this makes C-S-H one of the most abundant man-made materials in the world, some aspects regarding the kinetics, growth mechanisms and atomistic modelling remain as subjects of debate. In this section, a detailed description regarding the state-of-the-art knowledge about C-S-H is going to be exposed, focusing on the parts which are within the scope of this project and that are indispensable to help build upon.

In real Portland cements, C-S-H tends to grow from the alite grains, during the reaction of hydration. The hydration of alite reacting onto C-S-H can be described as it follows:

$$C_3S + (3 - x + y)H \rightarrow C_xSH_y + (3 - x)CH$$
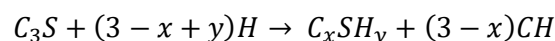
C-S-H phases are rich in Ca and Si. In real Portland cements it has a Ca:Si ratio of 1.75 at early stages of hardening, and also a variable water content in its inner structure. [26] It is important to note that C-S-H precipitates at the same time as some of the other hydration products such as ettringite, calcium carbonate $CaCO_3$ or portlandite $Ca(OH)_2$. [27]

2.2.2 The needle model

In her thesis, *Bazzoni* studied the hydration of the alite grain, describing the behaviour of the C-S-H during the different stages of hydration. [3] Later, endorsed by this thesis and new experimental data (a wider set of experiments than any other used for testing alite hydration models before), *Ouzia et al.* developed a model that describes the nucleation and growth of C-S-H; the so-called "needle model". [28]

EPFL

The model explains how, in early stages of hydration, C-S-H tends to grow from the surface of the alite grain in a shape that was first described as "needles", but that looks more like nanofoils or nanoribbons.

Moreover, it indicates that the heat peak in the calorimetry curve (the peak that separates the acceleration from the deceleration stage) is the time in which most of the nanoribbons have already nucleated and are in their fast growth period. Beyond this point, most of the surface of the alite is filled and the ribbons gradually enter their slow growth period.

There is also a clear differentiation between "inner" and "outer" C-S-H. The outer C-S-H is the first one to precipitate and it grows in shapes of nanoribbons. Once the surface is covered, inner C-S-H starts precipitating in the interlayer between the outer C-S-H and the alite grain. Because it grows slower, the contribution of the inner C-S-H can be negligible during the first part of the deceleration period and would only start contributing to the heat release from 20 h on. [28] In Figure 3 it is shown a SEM observation of the alite grain, where it can be examined the outer C-S-H and a well-developed layer of inner C-S-H in contact with the alite grain.
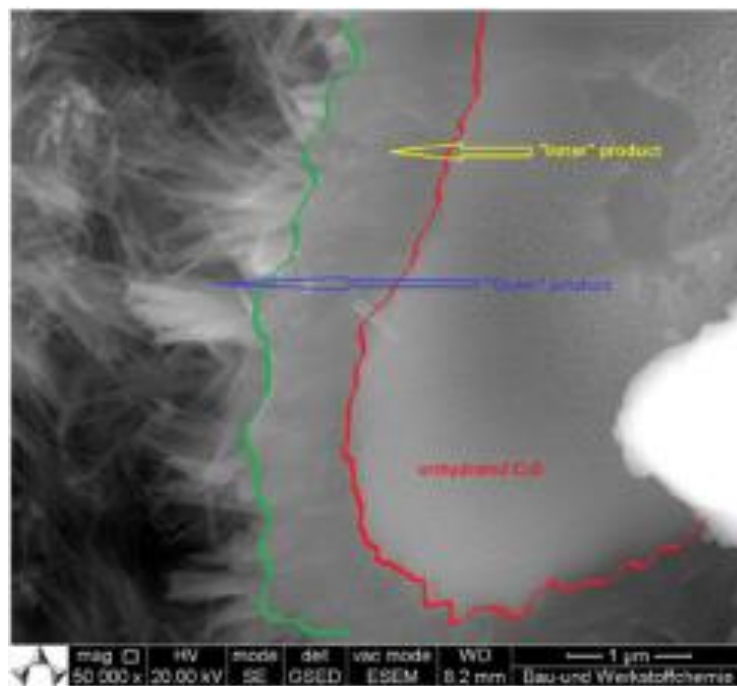
Figure 3: SEM observation of the alite surface after 4 days hydration. Outer (blue arrow) and inner (yellow arrow) C-S-H can be observed. [29]

Moreover, in the work done by *Tajuelo et al*. it is detailed how the morphology of C-S-H can change depending on the lime concentration, rather than the kinetics of hydration. [30] Samples synthesised at low lime concentrations in solution, i.e., [CaO] < 22 mmol/L, are foil like, whereas at higher concentrations ([CaO] > 22 mmol/L) the morphology is mainly fibrillar. Differences can be observed in Figure 4.

EPFL
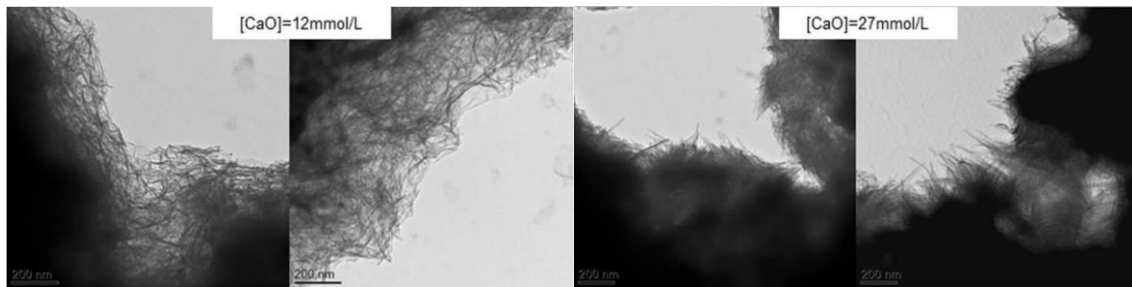
Figure 4: TEM micrographs of C-S-H samples produced by hydration of C_3S at a lower (left) and higher (right) CaO concentration. [30]

2.2.3 Synthetic C-S-H

So far it has only been exposed the C-S-H nucleation and growth in real cement conditions, meaning C-S-H grows from the surface of the alite grain. However, in real conditions C-S-H precipitates at the same time as other cementitious phases. Therefore, to distinguish the effects that the uptake of zinc may have it would be necessary to synthesize C-S-H as a single phase.

During decades, it was believed not to be possible to synthesize pure C-S-H alone at Ca:Si ratio above 1.5, which is a lower value than the ones for real cementitious systems (typically 1.75 or higher). Nevertheless, in recent years, the study initiated by *Kumar et al.* [31] and expanded by *Harris et al.* [32], proved that it was possible to synthesize pure C-S-H with Ca:Si ratios up to 2. The method for C-S-H precipitation is the one used in this thesis, and it is further explained in Section 3.1.2.

Synthetic C-S-H has a different aspect than the one of real cements, as it does not have the surface of the alite grain to grow from. Instead, it is formed through a pore solution in which sodium silicate and calcium nitrate react. The resulting C-S-H has as a nanofoil morphology, [31] similar to those shown by *Tajuelo et al.* at [CaO] concentrations below 22 mmol/L. [30] As it can be observed in Figure 5, synthetic C-S-H particles at higher Ca:Si ratio look like folded foils in contrast to the nanoribbon-like morphology of C-S-H in real systems, possibly due to the lack of heterogeneous nucleation points.
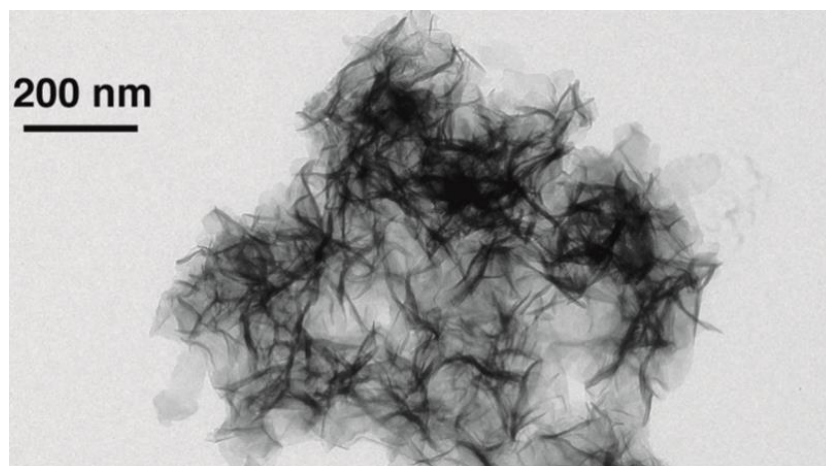
Figure 5: TEM image of pure C−S−H with Ca:Si ratio of 2, showing its nanofoil morphology. [31]

EPFL

2.2.4 The atomistic model for C-S-H

C-S-H is a poorly crystalline material and, thus, it does not have a long-range order. [33] Because of that, the approaches for obtaining the atomistic modelling were supported by Nuclear Magnetic Resonance (NMR) Spectroscopy. Combining these results with molecular dynamics simulations allowed *Kumar et al.* to propose the current atomistic model of C-S-H, [31] which can be observed in Figure 6.
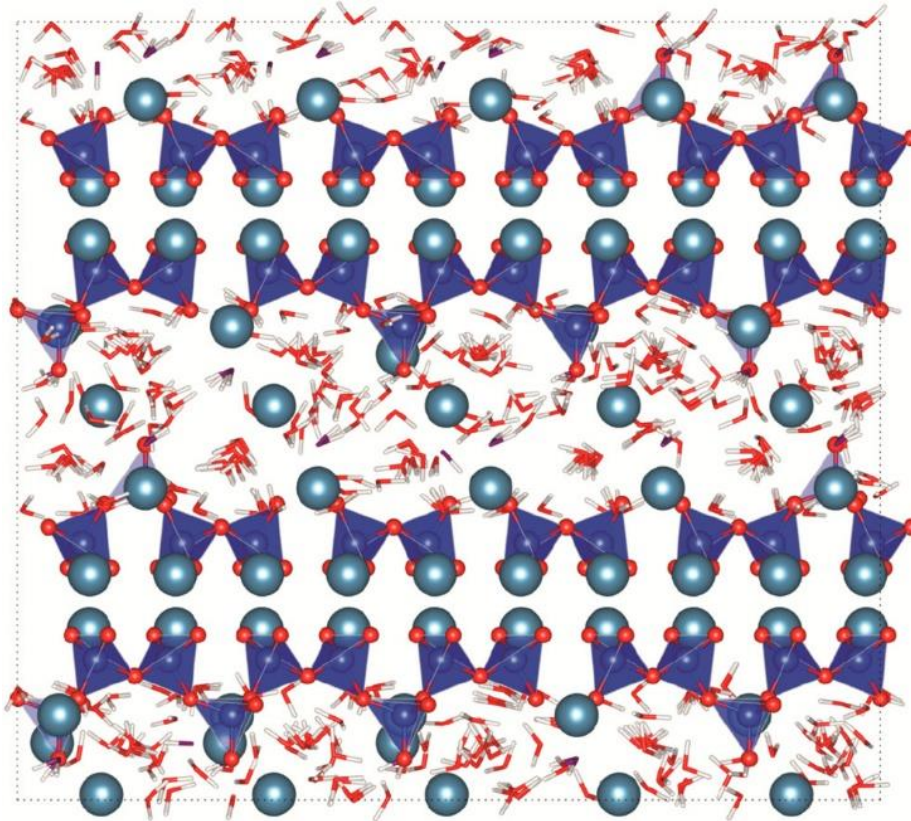
Figure 6: Structure of C-S-H for a Ca:Si ratio of 1.5. There are silicate dimers (81%), pentamers (14%), octamers (3%), undecamers (1%), and tetradecamers (1%). [31]

C-S-H atomic structure can be assimilated to that of a defective Tobermorite-14A (see Figure 7), consisting in a layered silicate structure spaced 14Å that allows water and calcium in the interlayers. There are three main silicates sites. The first ones are named Q1 sites and are in the end of the chain. The second ones are named Q2p (pairing sites) and exist only in molecules that are pentamers or larger, connecting the Q1 sites with the Q2b sites. Last, the Q2b sites (bridging sites) connect two Q2p sites. Calcium can be found in the interlayer, in the silicate chain, substituting for Q2b sites, and in the main CaO layer, as described in Figure 7. [31]

EPFL
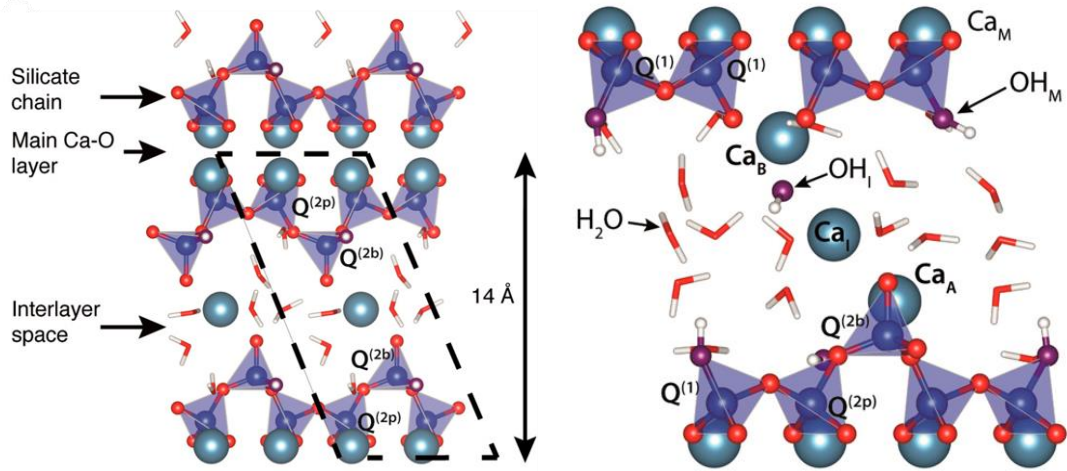
Figure 7: Chain topology of 14Å Tobermorite with Ca:Si = 0.83 (left) and C-S-H chains, showing two dimers and one pentamer (right). [31]

2.2.5 The role of zinc in C-S-H

Earlier work from the 1980s on additives to improve cement properties was mainly focused on the overall blend rather than targeting one particular phase, [[34], [35]] unlike what is intended in this project.

In her work, *Bazzoni* et al. concluded that the reactivity of the alite grains was directly related with the uptake of zinc. [1] Additionally, *Ouzia et al.* confirmed the hypothesis discussed by *Bazzoni et al.* that the increase in the nanoribbon length is sufficient to explain the increase in the degree of hydration and heat flow. [28] Therefore, C-S-H having longer ribbons would imply a higher reactivity. Studies confirm that the C-S-H ribbons become longer when small amounts of zinc are added, [[1], [2]] a phenomenon that can be directly observed in the TEM pictures presented in Figure 8. In fact, in their study, *Li et al.* were able to demonstrate that zinc additions increased C-S-H reactivity not only in the main peak (as it is shown in Figure 8) but also in all stages of hydration. [2]
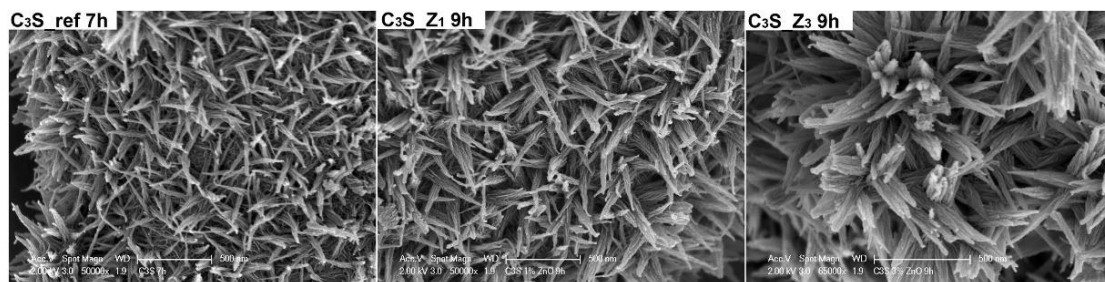
Figure 8: SEM images of hydrated samples at the peak of hydration. Nomenclature: C_3S (C_3S_ref), 1% ZnO doped C_3S ($C_3S\_Z_1$) and 3% ZnO doped C_3S ($C_3S\_Z_3$). [2]

More recent studies are being done to determine the atomistic structure of Zn-modified C-S-H. Results performed with NMR show that zinc modifies the chemical shifts of the different Si present in the C-S-H structure. This supports the theory that zinc is incorporated in the C-S-H structure. [36]

New NMR experiments were made to quantitatively assess the populations of Q species. Figure 9 shows a spectrum for Zn-modified C-S-H, and its deconvolution results. Apart from the three Si chemical shifts (corresponding to Q1, Q2p and Q2b) of C-S-H, in samples with zinc it was also found two new species in which zinc had changed the chemical environment of silicon. The current theory is that zinc would incorporate into the C-S-H structure in two different ways. First, it would substitute the silicon tetrahedra of the bridging site (Q2b), creating a new Si site that was named Q2p(Zn). Second, it can also substitute the silicon tetrahedra Q1 of the dimer, creating a new Si site that will be named Q*. [37]
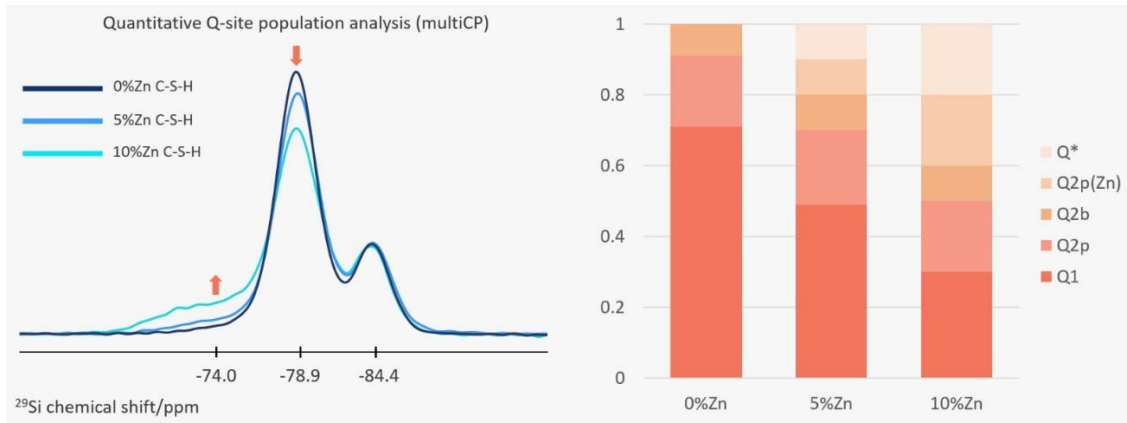
Figure 9: 29Si NMR spectra of three C-S-H samples containing different amounts of zinc (left) and its quantitative assessment of the samples' sites. [37]

To conclude with, smaller additions of zinc have proved to be beneficial regarding the reactivity of C-S-H. However, there are still lacking quantitative measures that support these studies and that can help give more accurate explanations regarding the effect of these minor additions. It is the aim of this project to further study the C-S-H behaviour in presence of zinc in order to get a full picture of the C-S-H characteristics.

3. Experimental methods

3.1 C-S-H Synthesis and handling

3.1.1 Reactants

The reactants used for C-S-H and Zn-modified C-S-H synthesis are the following:

- **Reactant 1:**
  - 10 mmol of sodium metasilicate (Na_2SiO, CAS: 6834-92-0).
- **Reactant 2:**
  - 20 mmol of calcium nitrate tetrahydrate ($Ca(NO_3)_2 \cdot 4H_2O$, CAS: 13477-34-4).
  - Different amounts of zinc nitrate hexahydrate ($Zn(NO_3)_2 \cdot 6H_2O$, CAS: 10196-18-6).

Both reactants 1 and 2 are dissolved in 200 ml of decarbonated water and have been supplied from Sigma-Aldrich. NaOH pellets (CAS: 1310-73-2) have also been used to prepare a 10 M solution in decarbonated water, and those were supplied from Acros Organics. Ethanol was supplied from Reactolab S.A.

3.1.2 Synthesis and handling method

The first step before performing all the different characterisation techniques is to synthesize single phase C-S-H in a reliable way. While *Kumar et al.* succeeding in producing high Ca:Si ratio C-S-H for the first time, [31] it wasn't until *Harris et al.* work that a reproducible method for producing pure C-S-H was properly described. [32] In this project, all C-S-H and Zn-modified C-S-H samples have been synthesized following their guidelines.

C-S-H is synthesized in a 12-cm diameter PMMA reactor that contains six free slots on top. Three of them have PMMA bars that increase turbulence during the mixing. Two other slots contain the inlet and outlet tubes for a continuous N_2 flow of 10 ml/min. The last slot is used to place a Mettler Toledo InLab Expert Pro ISM-P67 pH electrode, that monitors the temperature and pH values continuously during the reaction and displays them on the Mettler Toledo Easy Direct software. The reactor is placed in a water bath, which temperature is regulated by a thermostat at 19 ºC. The entire setup is shown in Figure 10.

EPFL
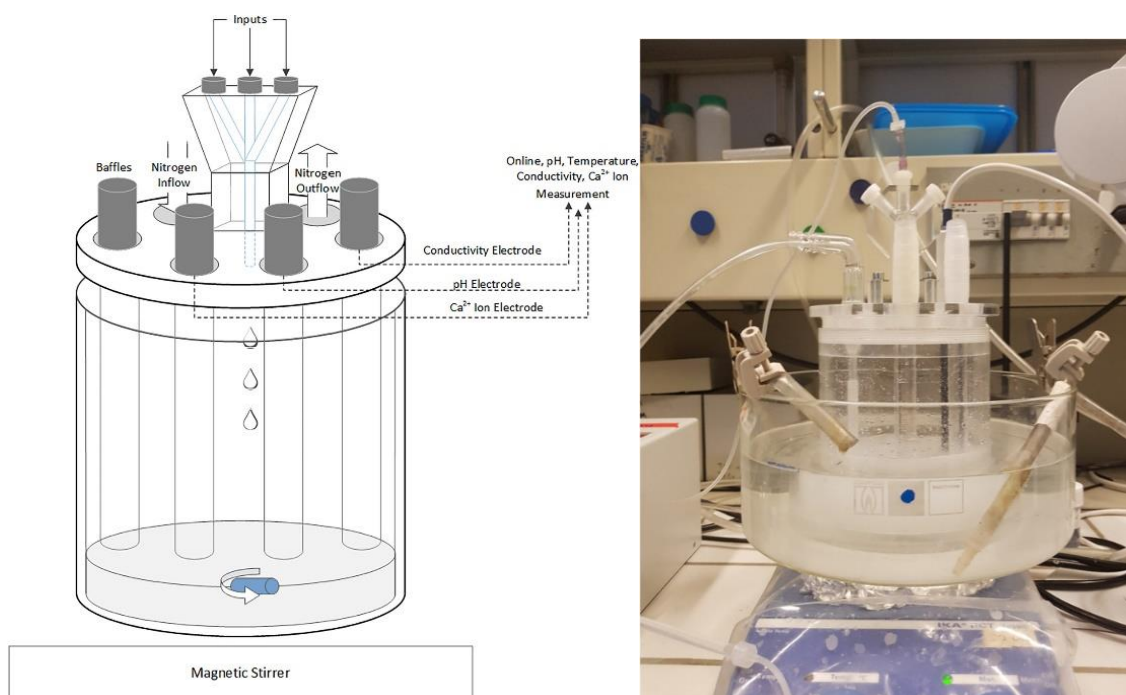
Figure 10: Scheme (left) and photograph (right) of the batch reactor for C-S-H synthesis. [32]

The solution containing Reactant 1 is poured in the reactor, altogether with a magnetic stirrer that mixes at 700 rpm. 7 ml of 10 M NaOH solutions is then decanted into the reactor and left for a minimum of 30 min to ensure the desired pH with an even distribution of NaOH. Once the reactor achieves the desired temperature, the stirrer is accelerated until 1100 rpm, speed at which is going to remain for the whole reaction. Then, Reactant 2 is pumped into the reactor at a rate of 2 ml/min throughout an ISMATEC REGLO-CPF Analog piston pump with an RH0.CTC pump head.

After at least 3h of reaction, the C-S-H solution is vacuum-filtered on a 200 nm filter paper (Whatman ME 24/21 STL). When only 100 ml remains unfiltered, 200 ml of supernatant is taken apart for further experiments. Then the filtration continues, and 60 ml of 1:1 ethanol and deionized water solution are added, so to remove salts and unwanted ions from the surfaces of C-S-H. Finally, the filtration is stopped when the C-S-H has completely precipitated with a wet paste consistency.

3.1.3 Products

When the filtering is over, the resulting C-S-H is stored half and half into two different vials, with their correspondent labels. The first vial is stored inside of a sealed bag and will not receive any further treatment; from now on this will be referred as "wet" C-S-H. The other vial is placed inside a freezer at -20 ºC for one day and then it is freeze-dried for 48 h in an Alpha 1-2 LDplus freeze dryer at -50 ºC and 0.01 mbar. The vial containing the resulting powder, from now on "dried" C-S-H, is stored inside of a sealed bag. The other product obtained is 200 ml of supernatant per batch, which is stored in properly labelled vials. The rest of the by-products are poured into a pH basic waste container for liquids.

It is relevant to note that, even if samples are synthesized without secondary phases, portlandite ($Ca(OH)_2$) or calcium carbonate ($CaCO_3$) can be formed in the drying, handling, or storage steps. [32] Therefore, samples will be further characterised throughout the two following techniques to check whether these phases exist or not.

3.2 Characterisation techniques

3.2.1 X-ray diffraction

X-ray diffraction (XRD) is a broadly used characterisation technique for phase identification, i.e., qualitative analysis, in cementitious materials. Amongst its several advantages, it can be highlighted the ease and the rapidness, as well as the reliable delivery of quantitative data that can be obtained. The diffraction of X-rays through the crystalline structure produces a pattern of peak positions and relative intensities that help identify the different crystal structures present in the sample. Qualitative analysis relies on comparing the peaks measured in the XRD pattern to those of known phases contained in a database. Since one peak at a certain diffraction angle can be identified as many different crystals, it is necessary to combine the database information with categorical or chemical filters, in order to restrict the number of candidate patterns. [38] As an example, in Figure 11 the diffractograms of four typical cements used in construction are presented.
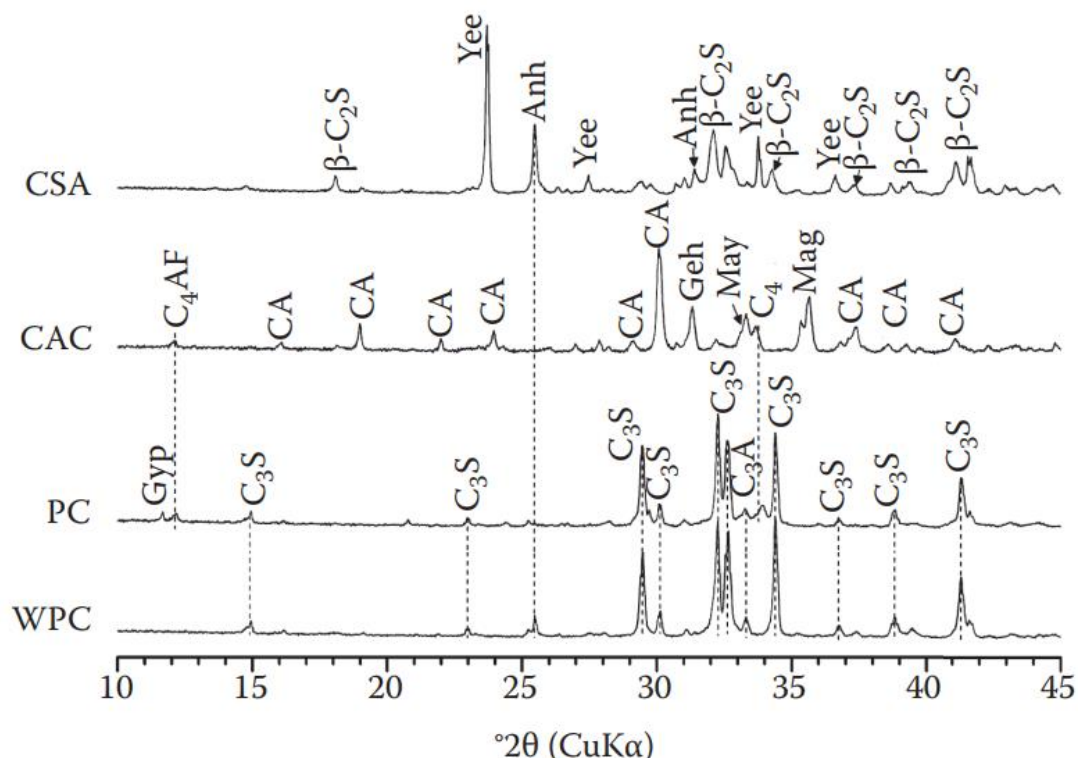
Figure 11: XRD scans of four classical cements: white portland cement (WPC), plain portland cement (PC), calcium aluminate cement (CAC) and calcium sulfoaluminate cement (CSA). The peaks phases include: alite (C3S M3), belite (β-C2S), aluminate (C3A), ferrite (C4AF), calcium aluminate (CA), ye'elimite (Yee), anhydrite (Anh), gypsum (Gyp), gehlenite (Geh), mayenite (May) and magnetite (Mag). [38]

Although it can also be used in quantitative phase analysis (QPA), in this project XRD is only performed for hydrated phase characterisation, in other words, to verify that the synthesized product is pure single-phase C-S-H and does not contain any traces of portlandite.

The experiment itself was carried out in a PANalytical X'pert X-ray diffractometer with an X'celerator detector using a double bounced monochromatic $CuK\alpha_{1,2}$ radiation and with a fixed divergence slit of ½. Every wet C-S-H sample was analysed at a range from $5°$ to $70°$ (2θ), with a step size of $0.017°$ for 30 min.

3.2.2 Thermogravimetric analysis

Thermogravimetric analysis (TGA) is a well-known characterisation technique for cementitious materials, often performed alongside with XRD to cross-check the presence of hydration phases. In this project, it is mainly going to be used to preliminary characterise the amount of bound water, carbonation and portlandite present in C-S-H samples. During TGA, samples are heated while weight loss is recorded. As temperature rises, the sample undergoes several thermal reactions (like dehydration or oxidation) associated with heat release or weight change. Temperatures in which these phenomena occur are characteristic for each mineral or hydrate. Therefore, by analysing the differential or derivative thermogravimetry (DTG) data, consecutive weight losses can be matched with different phases contained in the sample. [39] Figure 12 shows typical DTG plots for different hydration phases present in cement.
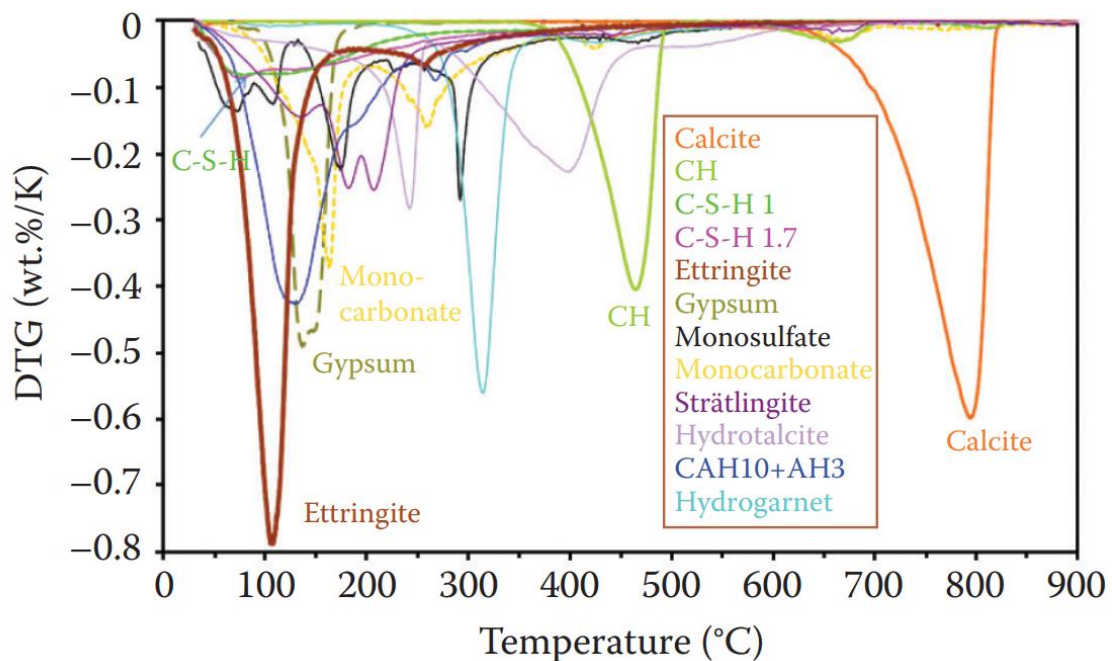
Figure 12: DTG examples of typical cementitious phases. [39]

In this project, the TGA experiment was performed by heating dried C-S-H samples (25 mg per sample) from $30°C$ to $1000°C$ at a rate of $10°C/min$ with a constant N_2 flow of 10 ml/min.

EPFL

The thermogravimeter, a Mettler Toledo AG (TGA/SDTA851e), recorded the curves of mass loss and their derivatives in function of temperature and time. Weight losses due to portlandite and calcium carbonate were analysed at intervals from 400ºC to 480ºC and from 600ºC to 710ºC respectively, with the tangent method for better precision. [39]

3.2.3 Laser diffraction

Particle size distribution (PSD) is one of the main ways of characterising powders, usually coupled with other techniques like TEM or SSA. Because many powders tend to aggregate (chemical bonding) or agglomerate (physical bonding like Van der Waals forces), it is highly advised that samples are always taken from a powder in motion and preferably in different intervals. [40]

Regarding PSD for cements, a very popular method nowadays is laser diffraction (LD). This technique measures the light scattered, adsorbed, and diffracted by a powder dispersed in liquid. Unlike others, LD can detect a wide range of powder sizes; from 1 to 1000 μm. The dilute suspension is placed in front of a laser light which gets scattered and collected at low angles. With this information, a volume distribution is calculated as a main outcome, alongside with other relevant results like the SSA (assuming a spherical particle shape). [40]

Samples were prepared by putting 50 mg of dried C-S-H in 50 ml of NaOH pH = 12. The powder was dispersed during 15 min with an ultrasonic horn (100 W, 200 kHz) and then 15 more minutes with a magnetic stirrer at 800 rpm, cooling down until room temperature. The refractive index selected for the powder was n = 1.596 (limestone as reference) and for the liquid n = 1.33 (water as reference). Also, the absorption coefficient chosen was k = 0.001. The experiments were performed in the Malvern Mastersizer S. device and the results were collected in its software. The obscuration factor, i.e., the percentage of laser light scattered by the particles, was set at a value of at least 12%, following the instrument's recommendations.

3.2.4 Specific surface area

Specific surface area (SSA) is a complementary parameter to PSD that gives further information about the fineness of a powder and its state of agglomeration. By itself, the SSA of a cementitious material has a direct influence on its hydration kinetics. For instance, in Figure 13, it is illustrated how a decrease in the particle size of alite, and consequently an increase of its SSA, implies an acceleration in its hydration. [40]

EPFL
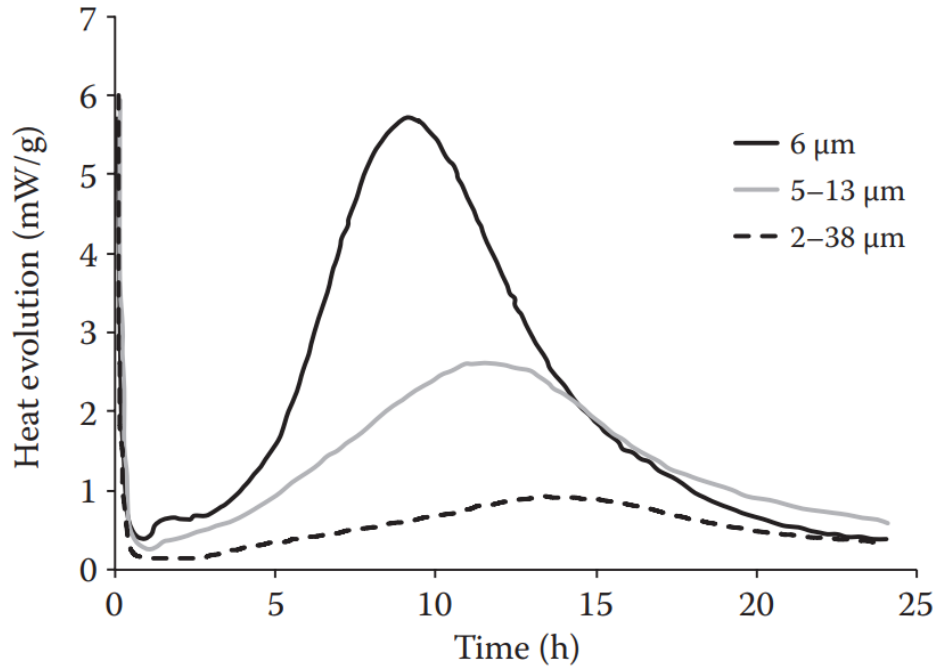
Figure 13: Effect of the PSD of alite on the heat evolution rate in hydrated pastes. [40]

Amongst the several methods used to obtain the SSA for cementitious materials, nitrogen adsorption is the preferable one. This is mainly because N_2 can access cracks, crevices and pores; places that with other traditional tests (like Blaine test) are not accessible. In the nitrogen adsorption technique, gas molecules are physically adsorbed onto the surface of the sample due to Van der Waals forces. So, to promote this process of adsorption, tests are carried out at cryogenic temperatures, usually with liquid nitrogen (-196ºC). Before the test, samples need to be degassed to remove physisorbed molecules (mainly water) from the surface. This procedure is not a trivial task and, if not performed correctly, it can become the main source of artefacts in the results obtained. It is thus important to have a standard procedure applied for every sample preparation.

In this project, samples were analysed in batches of three for higher consistency. First, three empty glass tubes with rubber plugs are placed and set to degas under a constant N_2 flow of 10 ml/min during 30 min at 110 ºC. Each of these tubes was then filled with 100 mg of dried C-S-H, stoppered with rubber plugs on top to avoid water readsorption from the atmosphere, and set to degas under the same N_2 flow during 2 h at 110 ºC. This values of time and temperature were determined by heating for a further 1 h at the same temperature and no further weight loss was observed, indicating that 2 h at 110 ºC under flowing nitrogen was sufficient. Once the samples were degassed, they were inserted into a Micromeritics TriStar II Plus machine with the tank full of liquid nitrogen and the test started. Samples have been analysed using the method based on BET's theory throughout the MicroActive for TriStar II Plus software. The degassing setup is shown in Figure 14.

EPFL
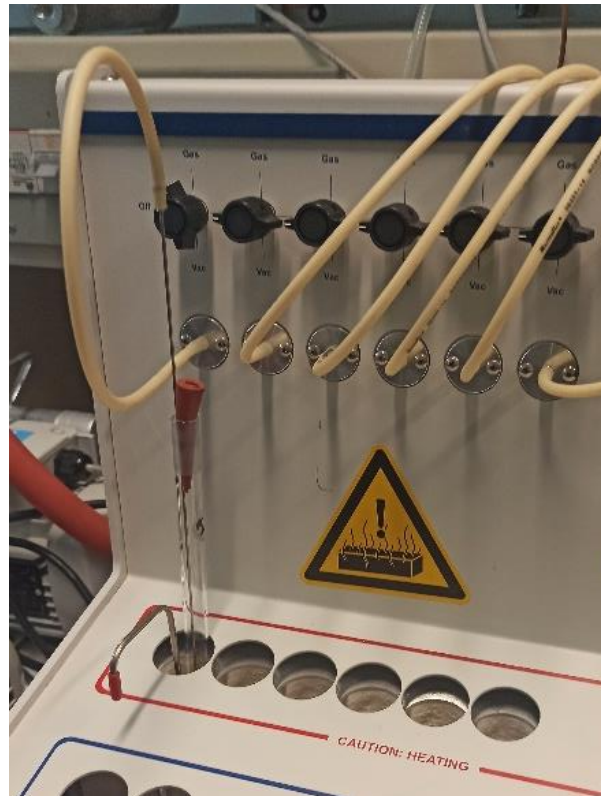
Figure 14: Degassing setup with the tube, the sample inside, the plug and the N2 lance.

To determine the SSA, the most accepted path is throughout the BET theory. It is based on the multilayer adsorption of gas molecules onto the adsorbent and involves several assumptions. [40] The BET equation can be expressed as it follows:

$$\frac{P}{V_a(P_0-P)} = \frac{1}{V_m C} + \frac{C-1}{V_m C}\left(\frac{P}{P_0}\right)$$ (Eq. 3.1)

P is the pressure of the gas in equilibrium with the sample, V_a is the amount of gas adsorbed at this pressure, P_0 is the saturation pressure of that gas, C is a constant and V_m is the quantity of gas necessary to cover the surface with a monolayer.
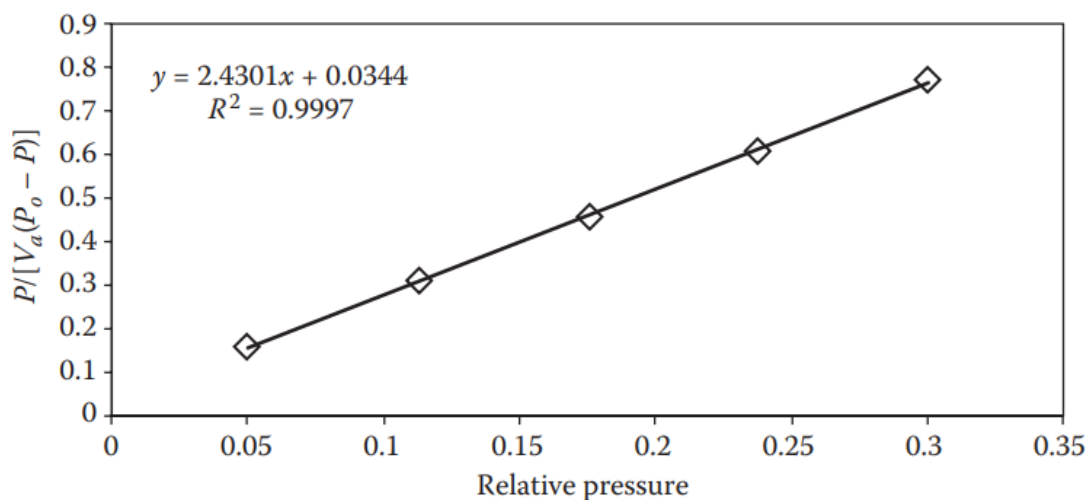
Figure 15: BET equation plot used to determine SSA. [40]

EPFL

The regression curve $P/[V_a(P_0-P)]$ vs. P/P_0 obtained from 5 points of the N_2 adsorption experiment should be linear, as illustrated in Figure 15. If so, not only can the model be validated, but also C and V_m values can be obtained by knowing the intercept and the slope. Having that, the SSA can be calculated with the following formula:

$$S_{BET} = \frac{N_A V_m A_N}{V_0}$$ (Eq. 3.2)

where N_A is the Avogadro constant and A_N is the area occupied by one gas molecule that is adsorbed. In the case of N_2, a value of $A_N = 16.2 \cdot 10^{-20}$ m^2 is normally assumed.

3.2.5 Zeta potential

Zeta potential, or ζ-potential, is the electrical potential at the slipping plane. This plane can be defined as the interface that separates mobile fluid from the stationary layer adhered to a dispersed colloid. Zeta potential is the scientific term for electrokinetic potential in colloidal dispersions. [42] It is thus measured in volts, or more commonly, millivolts. In general, if the zeta potential values are higher (positive or negative), it would imply that the medium (cations or anions respectively) are better adsorbed onto the surface of the suspended particle, or in other words, that the colloids are more stable in that medium. Therefore, zeta potential very much depends not only on the surface of the colloid, but also on the dispersion medium used. [43] A schematic representation of zeta potential is illustrated in Figure 16.
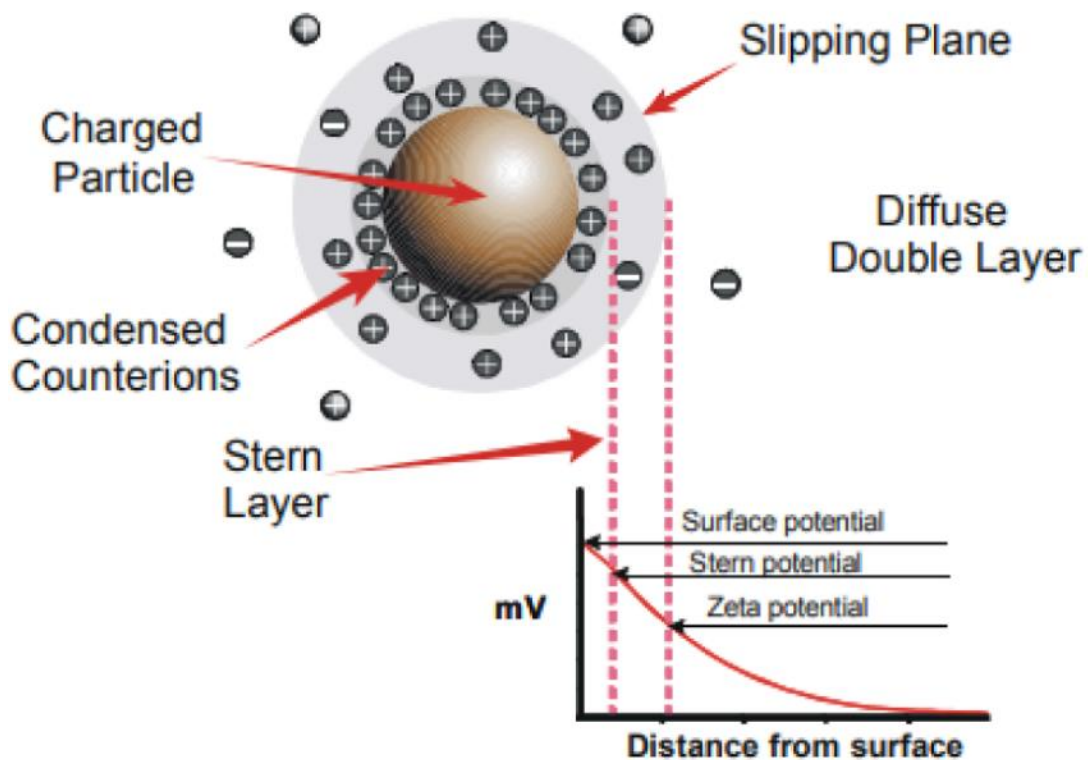
Figure 16: A schematic showing the zeta potential of a particle in a medium. [44]

EPFL

When applied to C-S-H, the zeta potential analysis can help elucidate the changes of its surface upon zinc incorporation. In this project, 4 g of wet C-S-H is dispersed into 160 ml of medium with a magnetic stirrer at 1100 rpm. The media used were a NaOH pH = 12 solution in water and the supernatant collected for each sample from the precipitation experiment. Measurements were done with the Colloidal Dynamics AcoustoSizer II device and collected in its own software. For every sample, 6 zeta potential measures were taken, one every 20 seconds.

3.2.6 Transmission electron microscopy

Electron microscopy is one of the most powerful techniques to study the morphology and composition of cementitious materials. It is mainly subdivided into scanning electron microscopy (SEM) and transmission electron microscopy (TEM). While the first one is easier to perform, it can only be used to observe the surface of the sample. Therefore, it is often used for evaluating surface fracture. On the other side, TEM is a much more delicate technique to perform, but its capability to observe the inner morphology of the sample makes it ideal to study the nanostructure of cementitious materials. Thanks to the powerful stationary electron beam shot directly into the sample, magnifications can be observed down few nm. [45]

However, there are many drawbacks related to this technique. First, due to the higher current density, C-S-H sample can get easily destroyed by excessive heating. Also, because of the high magnification and sample preparation, the field of view is limited. In conclusion, TEM images can be very accurate, but performing the experiments is not a trivial task. [45]

In this project, samples were prepared by dispersing 25 mg of "wet" C-S-H in 25 ml of isopropanol. Then, a drop of this suspension was set to dry on a 300-mesh copper grid under a lamp for an hour. Once dried, it is ready to be analysed with the TEM. The machine is a Tecnai OSIRIS TEM system (see Figure 17) which uses a FEI SmartCAM CCD camera to record the images. Samples are observed at 100 kV with a single tilt holder in bright field mode. The TEM measurements were performed by A. Morales.

EPFL
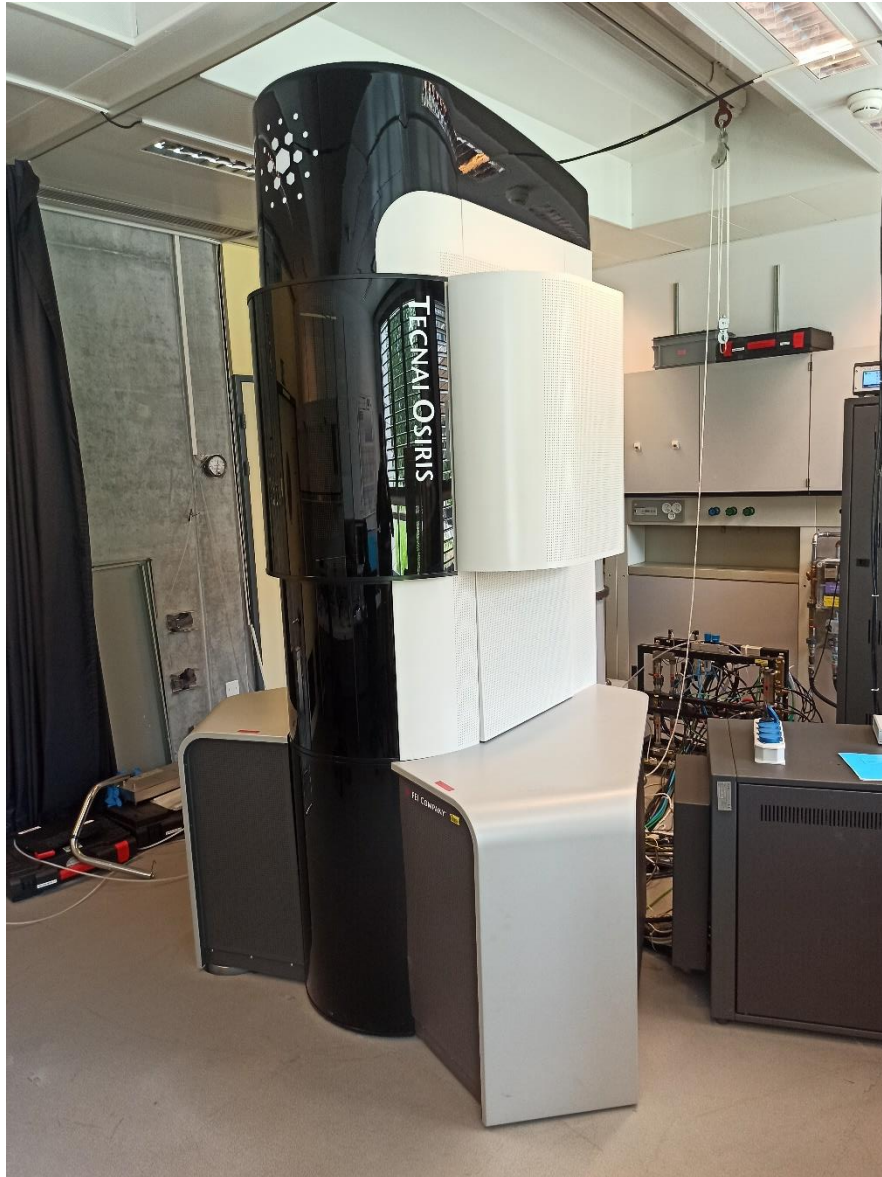
Figure 17: Tecnai OSIRIS TEM machine.

3.2.7 Optical microscopy

Optical microscopy (OM) is one of the oldest techniques used in scientific research, it was invented in the 18th century and is still in use today. The principle is very simple: by interposing a series of lenses between the viewers eyes and the sample, its microstructure can be examined in greater detail. Although OM is broadly used in scientific domains like microbiology, microelectronics and biotechnology, [46] in powder characterisation it is often on the backseat of other more powerful techniques such as SEM or TEM. This is mainly because it can reach a relatively low level of magnification with a decent accuracy; below 10 µm images are hard to interpret.

EPFL

Because of that, in this project optical microscope is only used to qualitatively observe the largest agglomerates that C-S-H may form. The procedure of sample preparation is going to be explained in light of the following results (see Section 4.3.2). All samples are observed in the Zeiss Axioplan optical microscope through the Zeiss Axiocam 105 color (see Figure 18) and analysed with the ZEN Widefield software. Lens magnifications used are 5x, 10x, 20x and 50x.

Figure 18: Zeiss Axioplan optical microscope.

4. Results and discussion

4.1 Samples preparation

Following the procedure presented in the Section 3.1.2, "wet" and "dried" samples of C-S-H with different amounts of zinc have been successfully synthesized, as well as 200 ml of supernatant per batch. All samples were prepared under such pH and temperature conditions that, as described in [32], targeted a final Ca:Si ratio of 1.75. Samples obtained are:

- Pure C-S-H.

- Zn-modified C-S-H with 0 Zn:Si.

- Zn-modified C-S-H with 0.15 Zn:Si.

- Zn-modified C-S-H with 0.2 Zn:Si.

- Zn-modified C-S-H with 0.3 Zn:Si.

- Zn-modified C-S-H with 0.4 Zn:Si.

4.2 Preliminary study

With all the samples prepared, the first concern was to check whether the method was correctly applied, i.e., the samples contained single-phase C-S-H. Therefore, a preliminary qualitative study including XRD, TGA and TEM was performed. Its aim is not only to corroborate the low or absent traces of portlandite and carbonation, but also observe if there are major differences between samples containing different amounts of zinc.

4.2.1 Characterisation through XRD

Figure 19 displays the diffractogram for the pure C-S-H sample. It can be observed the three main characteristic peaks at 29.4, 32.1 and 50.1 ± 0.1º that correspond to C-S-H. [38] The rest of the peaks are due to carbonation, even though with XRD it was not quantified the exact amount. Besides, no traces of portlandite were found.

EPFL
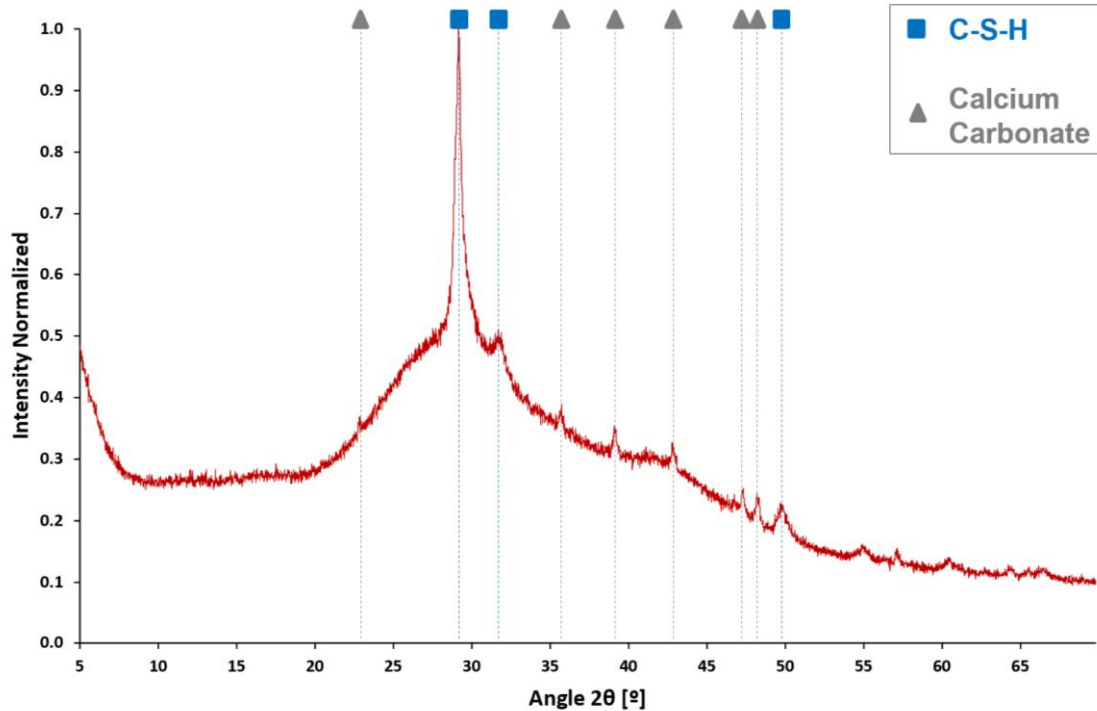
Figure 19: XRD diffractogram of pure C-S-H.

Analysing other samples, Figure 20 shows the XRD diffractogram for the Zn-modified C-S-H with 0.1 Zn:Si ratio. The three main C-S-H peaks appear again, while secondary peaks also show some carbonation. The main differences between this diffractogram and the one for pure C-S-H are the lower baseline and the sharper peaks. These differences exist because this last "wet" sample contained less water than the previous one due to the intrinsic variability of the drying process.

Same conclusions can be drawn from the analysis of the other four diffractograms (one per sample), which do not present any major differences between themselves. For the rest of the XRD diffractograms, the reader is refered to the Annexe of this report.

EPFL
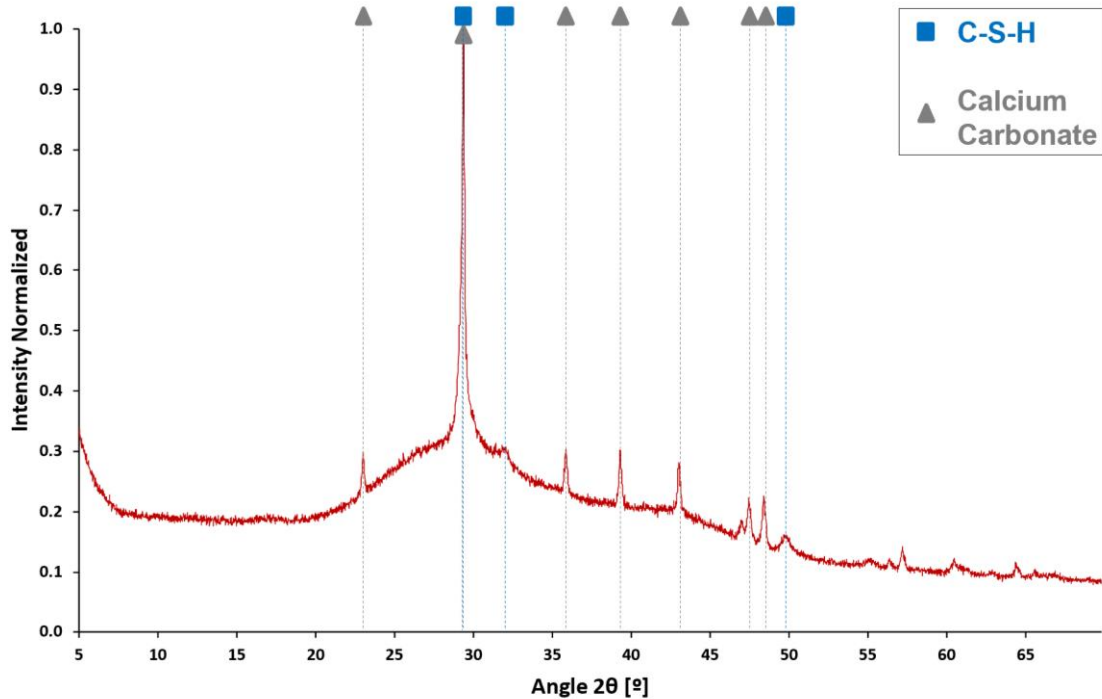
Figure 20: XRD diffractogram of Zn-modified C-S-H with 0.1 Zn:Si ratio.

Several conclusions arise from the XRD analysis. First, in all samples it can be observed small amounts of carbonation. This is difficult to avoid, as all C-S-H tends to carbonate on exposure to air during the sample handing, regardless of its Ca:Si ratio. [31]

Second, no portlandite is observed whatsoever. This does not imply that there is no presence of it in the samples; portlandite may exist in minor quantities below the normal detection limit.

Last, when studying the Zn-modified C-S-H samples, no new phases are observed. This supports the present hypothesis in which zinc is incorporated into the C-S-H structure and does not form separate phases. In other words, C-S-H remains C-S-H regardless of the zinc added up to the 0.4 Zn:Si investigated.

4.2.2 Characterisation through TGA

TGA experiments have been performed for all "dried" samples. The results, illustrated in Figure 21, have been normalised to be properly compared. It can be observed how samples lose weight continuously as temperature and time increase, until they reach a weight of around 75% of the original value. It seems that pure C-S-H behaves a little different than the rest, but other than that no major differences are observed.
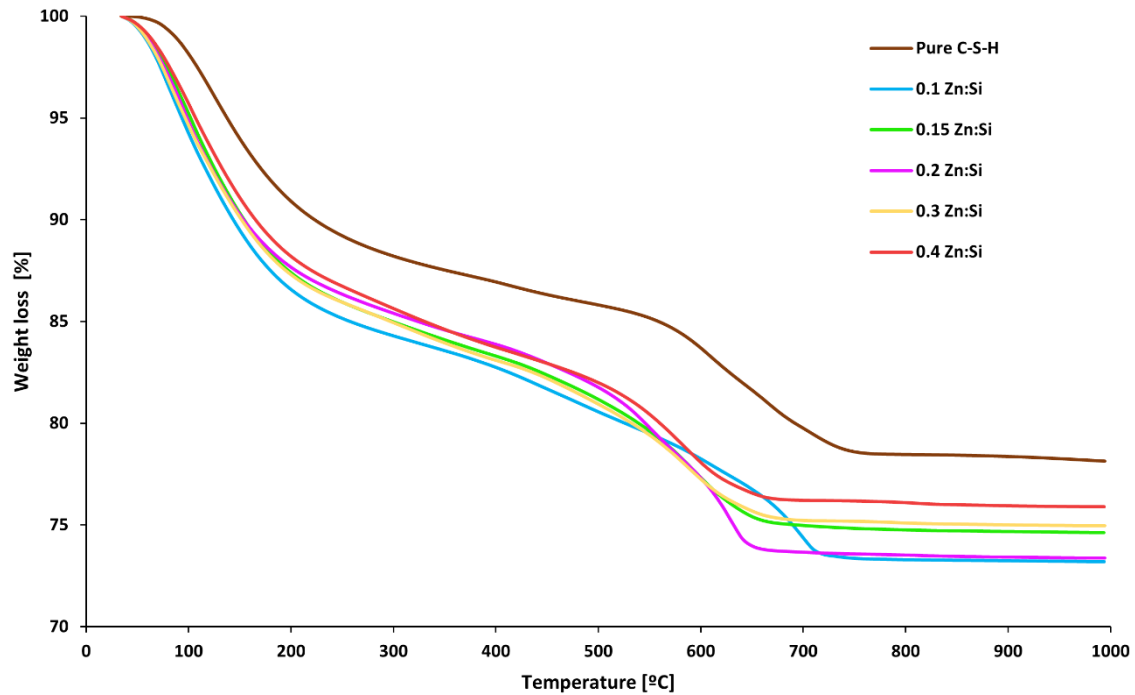
Figure 21: TGA plot for all C-S-H and Zn-modified C-S-H samples.

DTG plots for all samples are illustrated in Figure 22. In all of them, three main stages can be observed. There is a first clear change from 50 to 300 ºC that approximately corresponds to the loss of water contained in the C-S-H. [31] Note that, even though most of the bulk water is already evaporated from the sample because of the drying procedure, there is still some bound water in surface and in the inner structure of C-S-H; the one that corresponds to this first peak. More specifically, before the minimum value of the peak the weight loss would be due to loosely bound water evaporation whereas after the peak it would correspond to the strongly bound water (including the water in the interlayer) that is present in C-S-H.

Second, from 300 to 500 ºC there are some minor losses due to portlandite decomposition. This implies that there really are some minor traces of portlandite which could not be observed in the XRD.

Last, from 500 to 800 ºC, there is another clear peak that is directly related to decomposition due to presence of carbonates. This carbonation is likely to happen in C-S-H samples that have been exposed to air during the sample preparation. [32]

EPFL
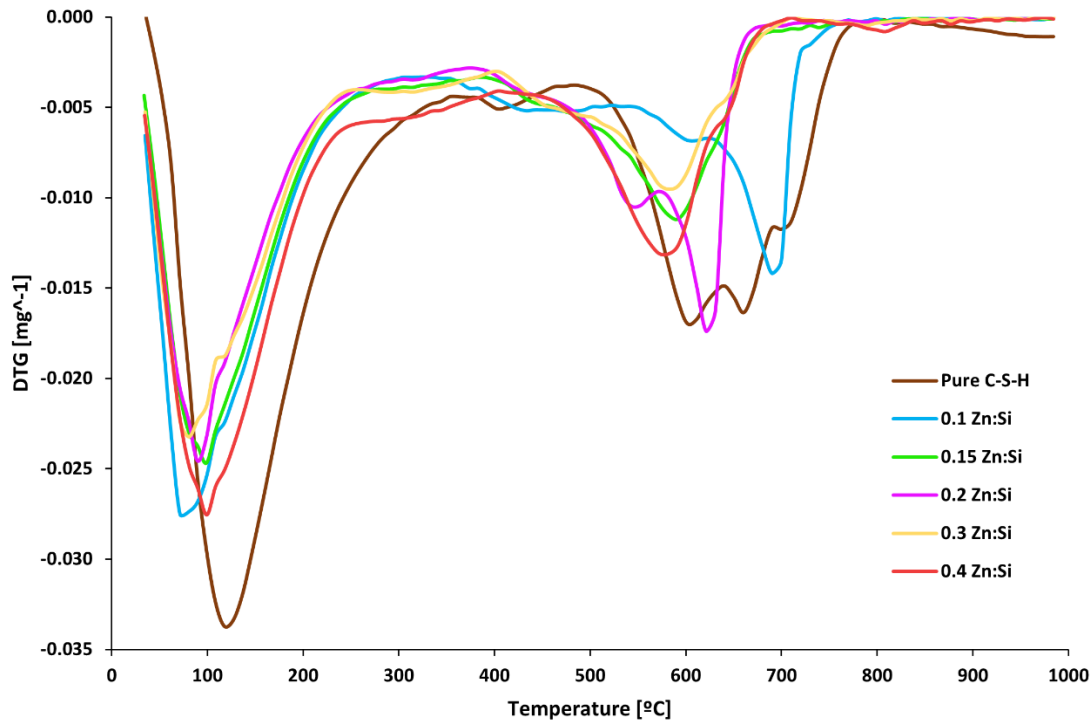
Figure 22: DTG plot for all C-S-H and Zn-modified C-S-H samples.

Thanks to the TGA analysis it has been demonstrated that minor amounts of portlandite also precipitated during the C-S-H synthesis. Relevant to note that, for Ca:Si ratios over 1.5, portlandite formation is more often observed, [32] making a bigger impact on the Ca:Si ratio of C-S-H. As concluded in the work done by *Harris et al.*, it is safe to assume that most of the carbonation being measured is of C-S-H itself, and not because of portlandite. Thus, it does not affect the C-S-H Ca:Si ratio before carbonation. [32] In other words, to recalculate the corrected Ca:Si ratio it is only needed to be subtracted the amount of portlandite from the overall mass. The obtained weight loss due to portlandite ($WL_{Ca(OH)_2}$) with the TGA and knowing the molecular masses of portlandite ($m_{Ca(OH)_2} = 74 \ g/mol$) and water ($m_{H_2O} = 18 \ g/mol$), the amount of portlandite present in each sample can be calculated with the following formula: [39]

$$Ca(OH)_{2,measured} = WL_{Ca(OH)_2} \cdot \frac{m_{Ca(OH)_2}}{m_{H_2O}} = WL_{Ca(OH)_2} \cdot \frac{74}{18} \qquad \text{(Eq. 4.1)}$$

Results regarding weight losses in TGA due to bound water, portlandite and calcium carbonate are shown in Table 1, as well as the recalculated Ca:Si ratio considering the targeted one of 1.75 and subtracting the portlandite amounts. It can be observed how portlandite formation during synthesis lowers the Ca:Si ratio. However, since the corrected Ca:Si ratio never gets below 1.7, it can be concluded that portlandite formation has a very small effect and, most relevant, samples being analysed still have a high Ca:Si ratio (i.e., >1.5). Overall, the results are consistent within the expected ones for C-S-H [32] and there is no clear difference or trend between samples with different amounts of zinc.

EPFL

Table 1: Percentage of weight losses obtained with TGA and recalculated Ca:Si ratio.

Sample	Bound water [%]	Calcium Carbonate [%]	Portlandite [%]	Corrected Ca:Si
Pure C-S-H	11.58	6.39	0.53	1.71
0.1 Zn:Si C-S-H	15.47	3.54	0.64	1.70
0.15 Zn:Si C-S-H	14.89	4.09	0.67	1.70
0.2 Zn:Si C-S-H	14.44	4.56	0.55	1.71
0.3 Zn:Si C-S-H	15.18	4.01	0.67	1.70
0.4 Zn:Si C-S-H	14.67	4.56	0.45	1.72

4.2.3 C-S-H imaging through TEM

Complementary to the previous sections, TEM was also performed for both C-S-H and Zn-modified C-S-H so to take a direct look at its morphology. Figure 23 shows two micrographs for pure C-S-H and two more for Zn-modified C-S-H with 0.4 Zn:Si. It can be observed how both C-S-H and Zn-modified C-S-H tend to aggregate with a nanofoil morphology, as discussed in Section 2.2.2.

Even though both present the nanofoil morphology characteristic for synthetic C-S-H which lacks heterogeneous nucleation points (those of the alite grain), the agglomerate structure of the sample containing zinc is not exactly the same. Regarding the TEM micrographs taken, Zn-modified C-S-H seems to have a much finer substructure, suggesting possible modifications in nucleation and growth mechanisms or kinetics. Moreover, in some parts of both Zn-modified C-S-H micrographs, agglomerates show a globular morphology, which contrasts with the main nanofoil one.

EPFL
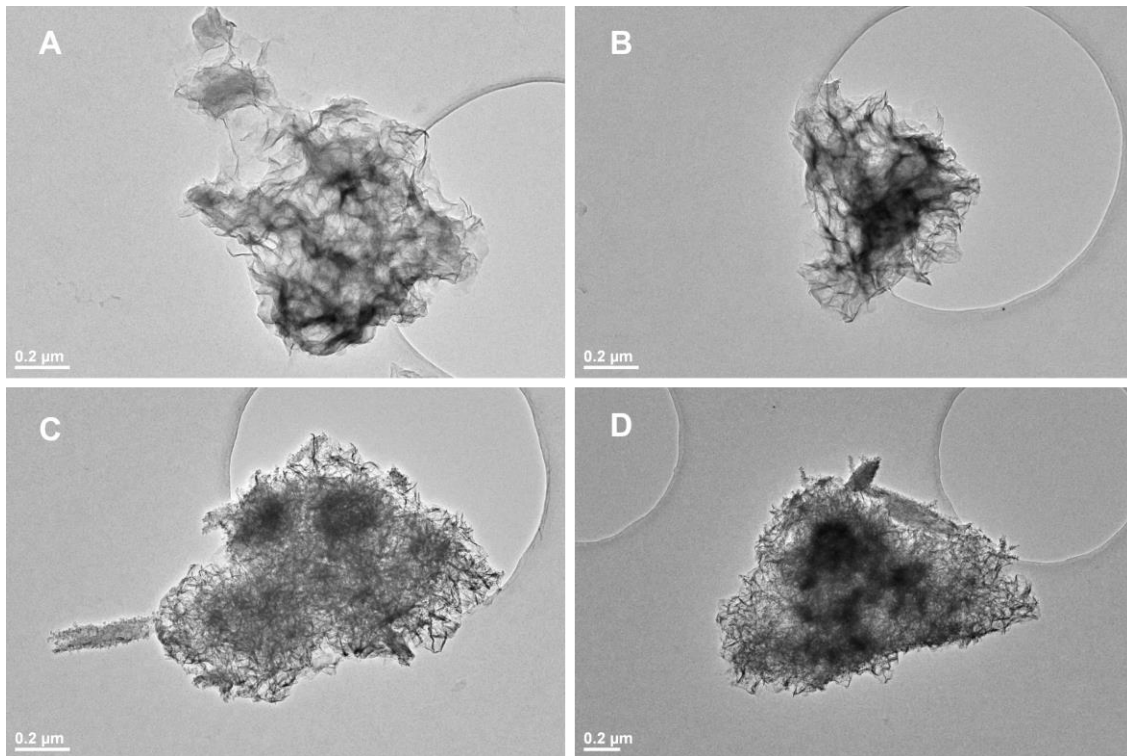
Figure 23: TEM micrographs for pure C-S-H (A and B) and Zn-modified C-S-H with 0.4 Zn:Si (C and D).

4.3 Particle size distribution

TEM imaging confirmed what was already mentioned in the state-of-the-art section: C-S-H tends to agglomerate. Having given an overview on its characterisation above, in this following section C-S-H will be studied in more depth through PSD and SSA measurements, so to obtain quantitative results that give more information about its state of agglomeration.

4.3.1 PSD through laser diffraction

Particle size distribution was performed using laser diffraction. The resulting frequency distribution curves for all different samples are shown in Figure 24. There are four visible modes at ~2.5, ~4.5, ~6.5 and between 40-60 µm. The two strongest modes can be observed for all samples, with two clear peaks at 4.9 and 6.6 µm, corresponding to two main families of agglomerates. To be noted that these two peaks remain in a similar position regardless of the amount of zinc. However, there is no clear effect of zinc in the height and sharpness of those peaks. In other words, no trend can be discerned with respect to different zinc contents.
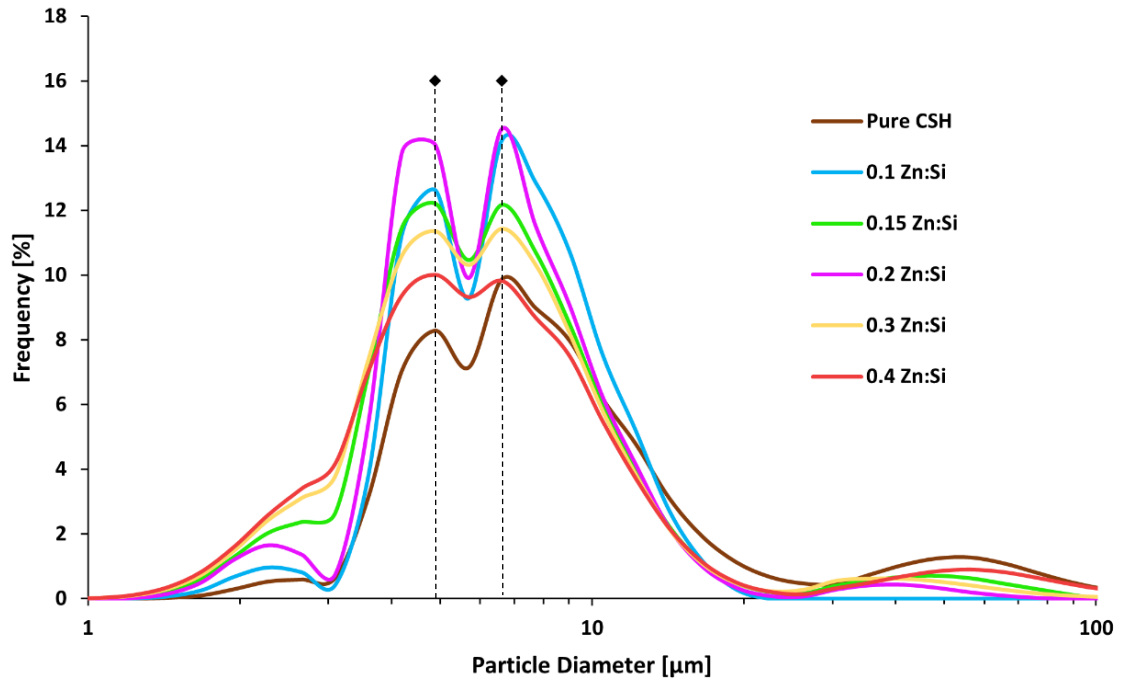
Figure 24: Frequency distribution for particle size of all C-S-H samples.

Following the guidelines exposed in [40], to better compare different PSDs the cumulative distributions of the previous frequency plot are shown in Figure 25. Same as the previous plot, all Zn-modified samples behave similarly, only for pure C-S-H is there a major difference. This is most probably due to an artifact in the handling or in the experiment performance, since it is detecting some agglomerates (>500 μm) that are a hundred times larger than the average ones. Furthermore, as it is stated in [40] and perfectly appliable in this case, tails of the PSD shall not be overinterpreted when particles are non-spherical. Either way, it can be concluded that both C-S-H and Zn-modified C-S-H tend to agglomerate in particles that are mainly between 1-20 μm large.

EPFL
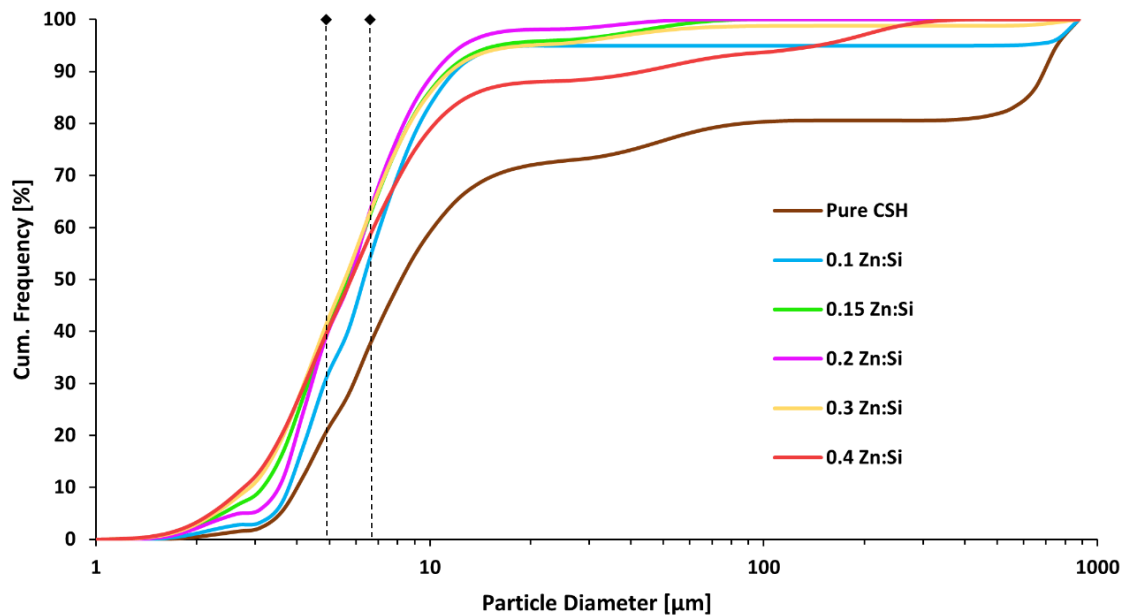
Figure 25: Cumulative distribution for particle size of all C-S-H samples.

When cross-checking the results with those of literature, it has been found that other works like [47] show similar results for mean particle size in synthetic C-S-H. However, these experiments are performed for low Ca:Si ratios (inferior to 1.4), and further studies with PSDs for higher Ca:Si ratios that corroborate the results of this project are yet to be done.

4.3.2 Optical microscopy for larger agglomerates

Despite being aware that tails in PSDs should not be overinterpreted, optical microscopy was performed in some C-S-H samples to check if these large agglomerates could be directly seen by lens magnification.

Samples are prepared in similar conditions as those of the LD: 50 mg of sample in 50 ml of NaOH pH = 12 solution, dispersed with the ultrasonic horn. However, instead of keeping the solution in movement to take a representative sample, it was left without stirring for two hours, so that the largest particles would sediment onto the base of the vial. After that time, the top liquid was poured away, leaving only the last 5 ml containing the C-S-H that sedimented with a little bit of dispersion medium. Then, one drop was extracted with a pipette and placed between two microscope slides to be observed.

Figure 26 shows two micrographs taken at 10 and 20 magnifications for the pure C-S-H sample. Also, Figure 27 shows the same but for the Zn-modified C-S-H with 0.4 Zn:Si sample. No major differences can be observed between both samples, and minor discrepancies can be attributed to sample preparation, an especially delicate procedure in this case as C-S-H tends to dry quickly. Large agglomerates of 50 µm can be observed in both cases, but no extra sized particles (around 1000 µm) were detected. With that, it can

be confirmed that the end-tails of the LD graph were due to an artifact, possibly gas bubbles.

However, in the micrographs shown it can also be observed a minor presence of tiny crystals, which are clearly not C-S-H particles. One hypothesis is that they might be salts formed during the synthesis process since the reactants contain sodium and nitrates, species that may react between themselves forming these crystalline structures. To prevent this salt precipitation, in the filtering process the C-S-H solution was washed with 60 ml of a 1:1 mixture of water and ethanol. To avoid further precipitations, special attention needs to be put in that step, maybe with a more in-depth washing procedure developed.
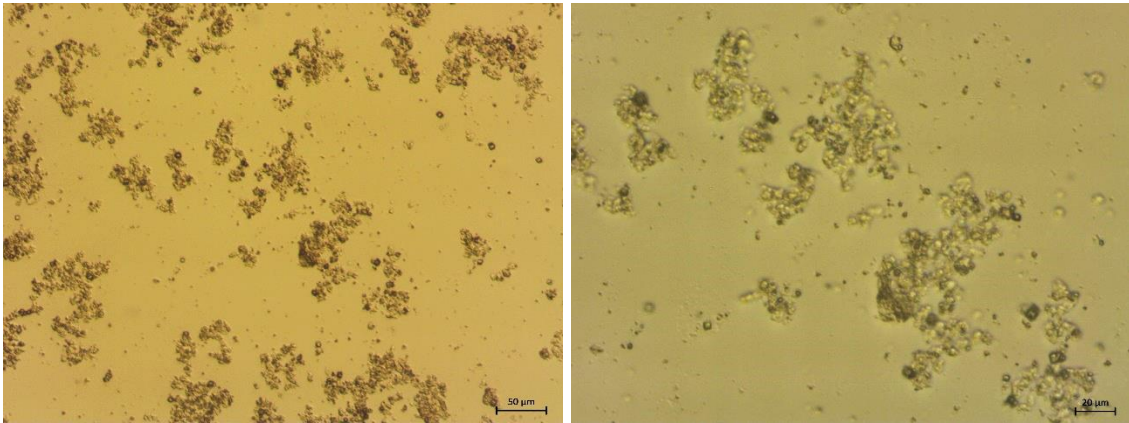
Figure 26: Micrographs of pure C-S-H diluted in a NaOH pH = 12 observed at 10x (left) and 20x (right) magnifications.
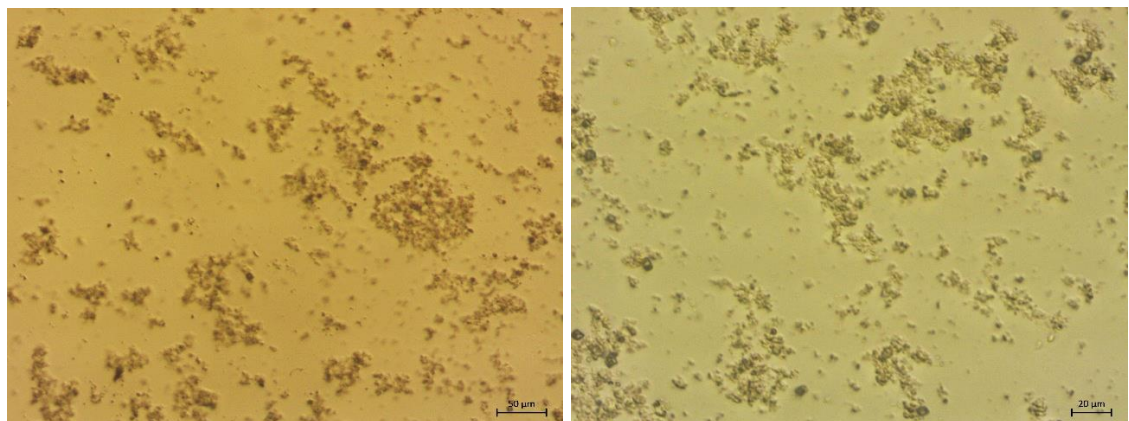
Figure 27: Micrographs of Zn-modified C-S-H with 0.4 Zn:Si diluted in a NaOH pH = 12 observed at 10x (left) and 20x (right) magnifications.

4.3.3 SSA through nitrogen adsorption

As mentioned, PSD is not enough by itself to characterise a powder, so it is usually coupled together with other techniques. [40] SSA results are expected to give further information about the state of agglomeration of C-S-H and Zn-modified C-S-H.

In the previous TGA analysis it was discussed how all samples would lose through evaporation its bound water at a range of temperatures from 50 to 200 ºC. Moreover, in Figure 22 it could be observed how most water loss peaks are at around 110 ºC. Before

EPFL

this threshold, the loosely (physically attached) bound water is evaporated; whereas beyond it, the water loss would be due to more chemically bond water, which could if removed compromise the inner structure of C-S-H. Therefore, the degassing conditions for the SSA experiments are set at this temperature of 110 ºC. These conclusions are consistent with the guidelines from literature, in which it is given an approximate value of 105 ºC for degassing conditions that target a removal of free water. [[39], [40]]

The obtention of the SSA through N_2 adsorption has only been performed for the pure C-S-H sample and Zn-modified C-S-H containing zinc with 0.15 and 0.4 Zn:Si. In the following Figure 28, Figure 29 and Figure 30 it is shown how the results agree with the BET model, as all plots follow a linear regression with goodness-of-fit measure of at least $R^2 = 0.9996$. In these figures the volume of N_2 adsorbed per gram of sample is shown and increases with the relative pressure. The variability of the results between the three samples of each batch is low (< 5%). Nevertheless, samples containing zinc show remarkably higher values of N_2 adsorbed per gram when compared to the pure C-S-H.

Figure 28: Validation of the BET model (left) and quantity of N_2 adsorbed vs. relative pressure (right) for pure C-S-H.

Figure 29: Validation of the BET model (left) and quantity of N_2 adsorbed vs. relative pressure (right) for Zn-modified C-S-H with 0.15 Zn:Si.
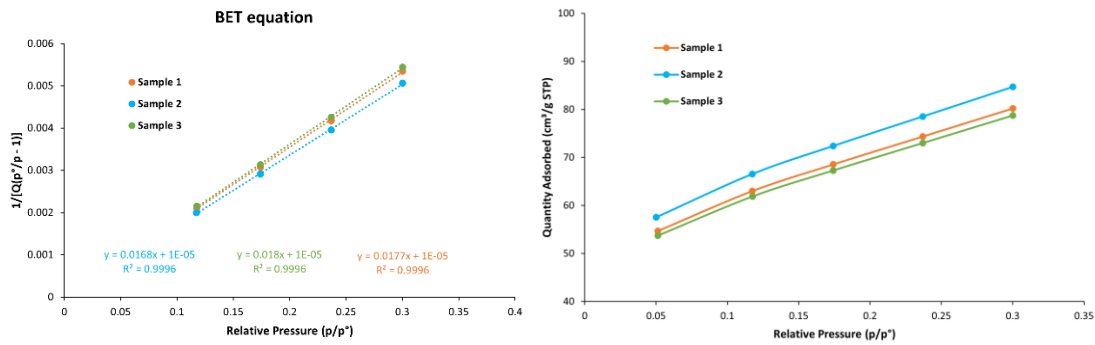
Figure 30: Validation of the BET model (left) and quantity of N_2 adsorbed vs. relative pressure (right) for Zn-modified C-S-H with 0.4 Zn:Si.
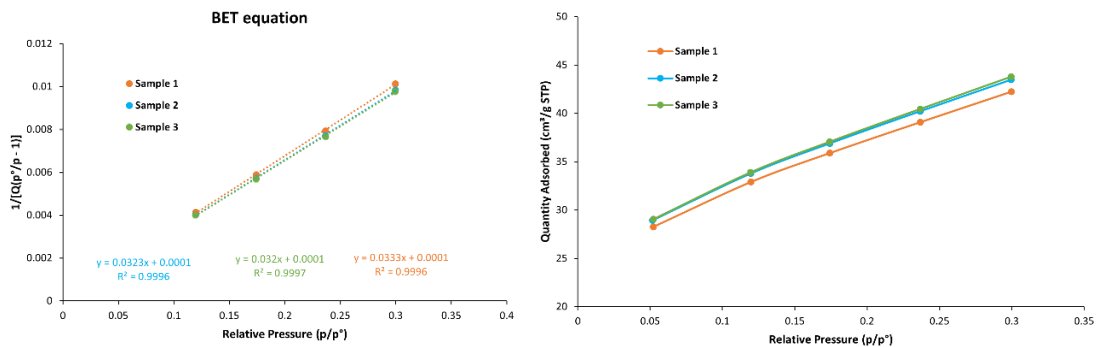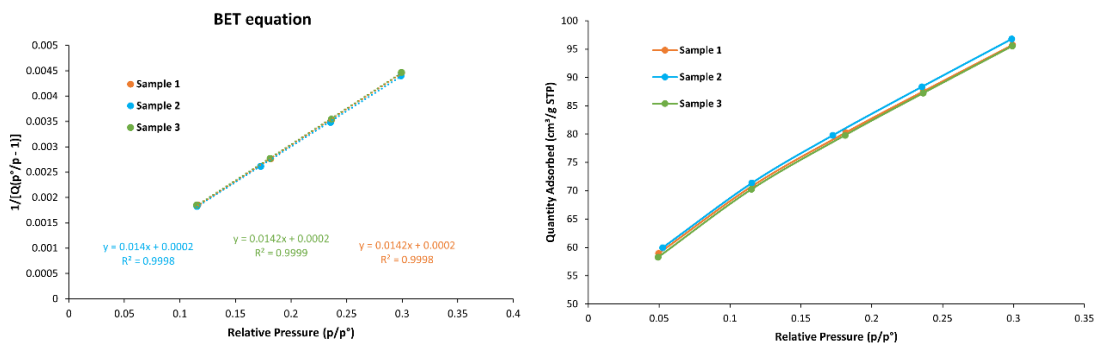
The SSA values results are summarized in Table 2, it can be observed that SSA values of samples from the same batch present a strong consistency with a low standard deviation between themselves, whereas SSA values between samples are really different. The addition of zinc onto the C-S-H may be a justification for that behaviour to some extent, but this dissimilarity is most probably due to a sampling error and/or enhanced during the handling procedure. As mentioned, degassing is a truly delicate procedure that is often the main source for artifacts in the results.

Table 2: SSA of Zn-modified C-S-H in function of different zinc amounts.

Zn:Si	Sample 1 [m²/g]	Sample 2 [m²/g]	Sample 3 [m²/g]	Average SSA [m²/g]	Standard Deviation [m²/g]
0	130.24	134.32	135.44	133.33	2.74
0.15	301.97	305.33	302.14	303.15	1.89
0.4	245.79	259.62	241.41	248.94	9.51
0.4	314.31 (2h)	317.42 (4h)	324.06 (6h)	318.59	4.98

To elucidate the possible impact of the degassing time in the results, a new experiment was designed. For Zn-modified C-S-H with a 0.4 Zn:Si ratio, the same procedure was repeated. This time, however, instead of doing the experiment for all three samples at once, every sample was analysed on its own with a different degassing time. Note that the degassing time for the first set of experiments was 2 h whereas in the following it was 2, 4 and 6 h.

The experiment was performed, the three regression lines agree with the BET model like the ones before and the results regarding the SSAs are illustrated in Figure 31 and in Table 2. This plot does seem to have a trend, with an increase of SSA as the degassing time gets longer. That is a logic phenomenon, as if the sample is exposed to a higher degassing time, more water will evaporate and therefore more room will be available for N_2 to adsorb. Then again, these results evidence that the degassing time is not the (only) source of artifacts in the results. First, because the SSA variations are not so broad compared to the bias

EPFL

between batches showed before. And second, because the SSA values shown on the table for the Zn-modified C-S-H with a 0.4 Zn:Si ratio are 70 m^2/g higher when compared to those of this last experiment, even though they are both the same material. Further investigation should be done in this direction to elucidate the causes for this inconsistent behaviour.
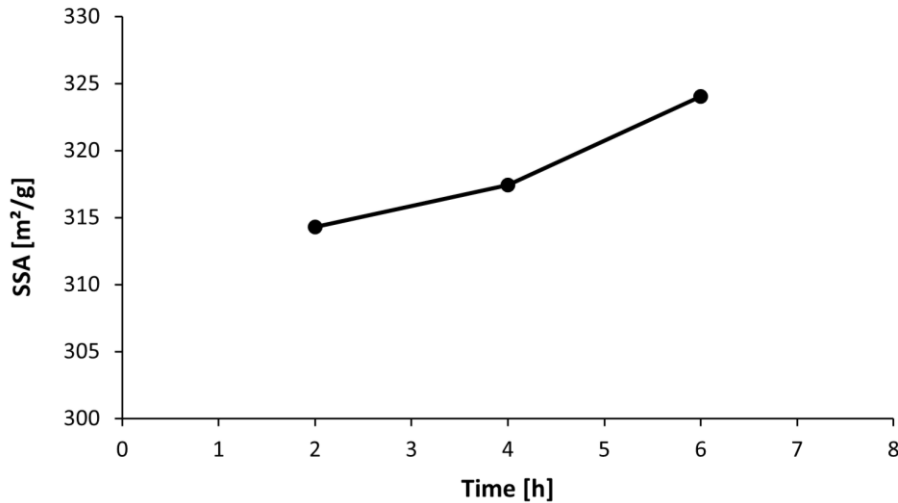
Figure 31: SSA of a Zn-modified C-S-H with 0.4 Zn:Si ratio at different degassing times.

All these SSA results can be cross-checked with previous atomistic simulations performed. [48] In literature, most SSA measurements are in the range of 200-300 m^2/g. [[49], [50]] This would correspond to the (001) model surface of two-interlayer thickness, which can be seen in Table 3. In the case of this project, the range is broader (133-303 m^2/g) and does not always coincide with the model, but still agrees with the computational approach in the fact that C-S-H is generally at least two interlayers thick.

Table 3: SSA of computational C-S-H surface models depending on the number of interlayers. [48]

Number of interlayers	SSA [m^2/g]
0	870
1	360
2	220
3	160
4	130

The results for the SSA through nitrogen adsorption and those of PSD can be used to estimate the state of agglomeration of C-S-H. One method is by calculating what is known as the agglomeration factor F_{AG} with the following formula: [40]

EPFL

$$F_{AG} = \frac{D_{v50}}{D_{BET}}$$ (Eq. 4.2)

D_{v50} is the median volume diameter in micrometres and is obtained from the cumulative plot of the PSD analysis (see Section 4.3.1). D_{BET} is an average diameter in micrometres calculated with the following formula, assuming foil-like morphology: [41]

$$D_{BET} = \frac{24}{SSA \cdot \rho}$$ (Eq. 4.3)

SSA is the average specific surface area calculated as already shown at Table 2 and the density is assumed as $\rho = 2.47$ g/cm^3 for freeze-dried C-S-H. [51]

The results for the agglomeration factor, as well as both diameters are shown in Table 4. With a range from 110 to 171, it can be concluded that the powder C-S-H and Zn-modified C-S-H is very heavily agglomerated. The range of values for the agglomeration factor is still broad due to the dispersed results obtained in the SSA measurements and the artifacts in the LD that affected the median diameter. Still, if the variability is reduced and reproducibility improved, the range could be narrowed down.

Table 4: Agglomeration factor of Zn-modified C-S-H in function of the different amounts of zinc.

Zn:Si	Average SSA [m²/g]	D_{BET} [μm]	D_{v50} [μm]	F_{AG}
0	133.33	0.075	8.25	109.98
0.15	303.15	0.033	5.65	171.39
0.4	248.94	0.040	5.80	144.32

4.4 Surface behaviour – A zeta potential approach

Having already studied the particle size distribution of C-S-H and discussed its state of agglomeration, this project will be concluded with an inspection to its surface behaviour. In this section, zeta potential measurements were performed for all samples in two different media, so to compare both results.

The first round of experiments was performed with C-S-H dispersed in a NaOH pH = 12 solution. Six measures were taken in each case and the zeta potential was obtained using the Smoluchowski approximation. The average of these six measures, as well as the error bars (maximum and minimum values) are displayed in Figure 32. It can be observed how all zeta potential measurements are above 0 mV, which would mean that both C-S-H and Zn-modified C-S-H terminate positively. Since in the dispersion medium there are only Na$^+$ and (OH)$^-$ ions, it is possible that C-S-H tends to attract these positive sodium ions that get adsorbed onto the surface. Nonetheless, zeta potential values are overall low, which means

EPFL

that this effect would be rather weak. Also, when comparing the results for the C-S-H with the Zn-modified one, the latter gives slightly higher values. Since the difference is ≤ 1 mV, the experimental evidence is not enough to draw further conclusions.
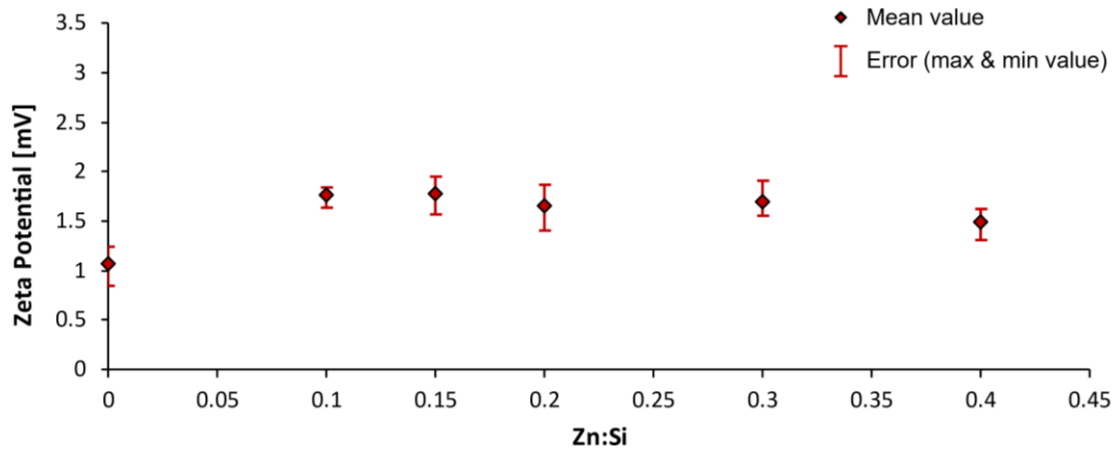
Figure 32: Zeta potential measures, with average and error bars, for all C-S-H and Zn-modified C-S-H samples. Dispersion medium: NaOH (pH = 12).

A second round of experiments were performed under the same conditions, but each sample was dispersed in its own supernatant (pH = 13.1) instead of the NaOH solution. The results are summarized in Figure 33. There are two main changes when compared to the previous ones. First, all zeta potentials are one order of magnitude above, i.e., now results oscillate between 17 and 24 mV. Second, the trend has been inverted and the pure C-S-H presents a higher zeta potential values than those containing zinc.
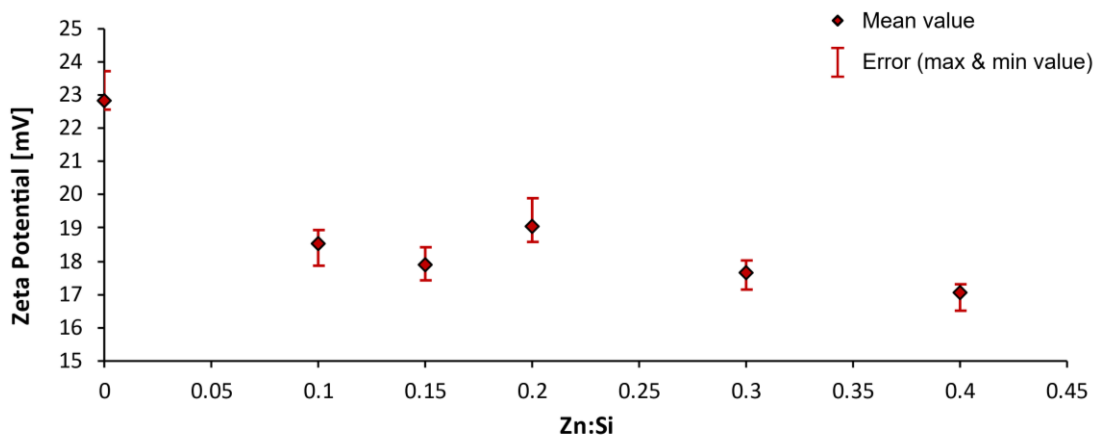
Figure 33: Zeta potential measures, with average and error bars, for all C-S-H and Zn-modified C-S-H samples. Dispersion medium: supernatant of each sample (pH = 13.1).

All results of the two previous figures are consistent with previous studies performed in the laboratory. Those concluded that pure C-S-H with Ca:Si = 1.75 has zeta potential values lower than 4 mV when dispersed in NaOH solution at pH = 12, and lower than 30 mV when dispersed in supernatant at pH = 13. [52]

EPFL

Taking a deeper look into the results for the samples dispersed in supernatant, the fact that they present higher zeta potential values than those in the NaOH solution can be explained by a combined effect of a raise in pH and an increase of Ca^{+2} concentration in solution. On the one hand, it has been shown through titration that, for C-S-H dispersed in supernatant, zeta potential increases with pH. [52] On the other hand, regarding the effect of the ions in solution, the supernatant contains higher concentrations of Ca^{+2} than the NaOH solution (which contains none). Several studies have concluded that the zeta potential increases alongside with the Ca^{+2} concentration in the dispersion media because the calcium tends to accumulate near the surface of C-S-H. [[53], [54]] Moreover, it is also known that Ca^{+2} adsorption is favoured over alkaline ions when they are competing under similar concentrations. [48] This would explain why the zeta potential is significantly higher in supernatant, a media which contains both Ca^{+2} ions and Na^+ ions from the reactants.

The other main different behaviour mentioned is the clear drop in zeta potential values once the C-S-H uptakes zinc. Currently, there is investigation being carried out in the Minor Elements Project regarding the atomistic modelling of Zn-modified C-S-H. Evidence suggests that zinc might be part of the surface, substituting some of the silicon atoms or Ca^{+2} ions in surface bridging sites. [48] If this is the case, it is coherent to argue that the surface may accommodate less Ca^{+2} ions, lowering consequently the zeta potential of the Zn-modified C-S-H, as shown in the experimental results.

All in all, these experimental results regarding zeta potential are consistent with other studies performed in the laboratory [[36], [37], [48], [52]] that led to the current hypothesis exposed in Section 2.2.5.

EPFL

5. Conclusions

The aim of this thesis was to study the C-S-H with and without the uptake of zinc to obtain a broader picture of its structure, state of agglomeration and surface behaviour; as well as characterising the impact of zinc uptake in its general physical properties. In the following section, a final overview with the main conclusions will be given.

C-S-H and Zn-modified C-S-H at high Ca:Si ratios (>1.5) was successfully synthesized through the dropwise precipitation method exposed in [32]. Samples with different amounts of zinc additions (Zn:Si, between 0.1 and 0.4) were prepared for the experiments.

The analysis with the XRD confirmed that all samples were single-phase C-S-H with very small amounts of carbonation that most likely occurred during handling process. Moreover, it confirmed that zinc was incorporated onto the structure of C-S-H and no new phases were formed. Complementary to this, TGA quantified the bound water, carbonation and portlandite losses. Thanks to that, it could be confirmed that Ca:Si ratio does not decrease below 1.7 due to portlandite formation, which implies that the C-S-H samples are still in the range of high Ca:Si ratios. Also, TGA's bound water peak at 110ºC set the degassing temperature for the following SSA experiments. Regarding TEM imaging, it confirmed the foil-like morphology of C-S-H showed in previous studies. However, no differences could be observed between C-S-H and Zn-modified C-S-H.

The PSD through laser diffraction (LD) showed two main families of agglomerates, with modes at 4.9 and 6.6 µm, that remained in a similar same position regardless of the amount of zinc added. PSD measurements showed that both C-S-H and Zn-modified C-S-H tend to agglomerate in particles that are 1-20 µm. Optical microscope allowed to directly observe these agglomerates but did not see agglomerates > 50 µm and showed that the artifacts seen in the end-tails of the PSD (> 300 µm) were not physical. Also, the optical microscopy showed significant quantities of salt crystals (normally $NaNO_3$) suggesting incomplete washing of the precipitated C-S-H. The state of agglomeration was further studied with the obtention of the specific surface areas (SSA) through N_2 adsorption using the BET model. SSA values oscillated between 133 and 325 m^2/g, with higher values for samples containing zinc. For the same sample (0.4 Zn:Si) a relative error > 20% was observed, much higher than expected and further work is needed to understand such variability. When the SSA values were compared with those of the atomistic modelling, they did not always agree as the range was too broad, but still agreed with C-S-H being around two interlayers thick. By crossing the SSA values with the previous PSD results, an agglomeration factor F_{AG} that ranged from 110 to 171 was calculated. The broadness of the range is influenced by the SSA values, which means that more accurate results could be obtained if the reproducibility regarding the N_2 adsorption experiment was improved. However, it can be concluded that C-S-H is a very heavy agglomerated powder.

Zeta potential experiment was performed firstly for samples diluted in NaOH pH = 12

EPFL

solution. The results were similar regardless of the zinc amounts; all of them positive but below 3 mV. Secondly, samples analysed when dispersed in supernatant presented significantly higher zeta potential values overall, from 17-24 mV. This can be explained by a combined effect of a raise in pH altogether with an increase of Ca^{+2} ions in solution. Also, the results showed how zeta potential decreased for Zn-modified C-S-H. This effect could be linked with the current theory of the C-S-H atomistic modelling, which would be that zinc substitutes both calcium atoms in the bridging site and silicon atoms in the surface of C-S-H. If so, it could reduce Ca^{+2} ions adsorption sites, which could explain why the zeta potential is lower.

For future perspective, a focus should be put in the reproducibility of the PSD and the SSA, with emphasis on the latter. Before analysing C-S-H with different amounts of zinc with the N_2 adsorption method, several samples of the same material should be analysed with the exact same degassing procedure to check which is the intrinsic variability of the experiment. For zeta potential experiments, they could be redone with dried C-S-H samples instead of wet ones and putting special focus in the dispersion procedure. Possible improvement of the washing step for the precipitated C-S-H could also be investigated.

Following these guidelines, further experimental results will help validate, corroborate, refute and/or expand the conclusions of the present thesis.

EPFL

Acknowledgements

First, I would like to thank Paul for the giving me the opportunity to join the PTG group and put my brick in this giant wall. During the days in the lab, his valuable advices helped me better interpret the results and orientate myself on what to do next.

Second, I would also like to thank Maya for the time spent together in the lab and in the office, where she helped me with everything she was able to. Her altruistic implication in the project was crucial for it being what is now.

Third, I cannot forget those who shared their time to aid me: Ziga, Jean, Lionel, Sarra and Diana; everyone brought their grain of sand to this thesis.

Last, I would like to make a special mention to Anna. She was the one who contacted and offered me this project in the first place, before we even met. Without that, I wouldn't have had the chance to come to Lausanne and live this experience. She has also been the one that has spent the most time with me in this project, and the one from which I learned the most. Her jovial and informal energy made me feel very comfortable and welcome in the lab.

Thanks to everyone.

EPFL

References

[1]   Bazzoni, A., Ma, S., Wang, Q., Shen, X., Cantoni, M., & Scrivener, K. L. (2014). *The Effect of Magnesium and Zinc Ions on the Hydration Kinetics of C3S*. Journal of the American Ceramic Society, 97(11), 3684–3693. https://doi.org/10.1111/jace.13156

[2]   Li, X., & Scrivener, K. L. (2022). *Impact of ZnO on C3S hydration and C-S-H morphology at early ages*. Cement and Concrete Research, 154, 106734. https://doi.org/10.1016/j.cemconres.2022.106734

[3]   Bazzoni, A., Scrivener, K., & Cantoni, M. (2014). *Study of early hydration mechanisms of cement by means of electron microscopy*. Lausanne, EPFL. https://doi.org/10.5075/epfl-thesis-6296

[4]   Rodgers, B. L. (2018, December 17). *Climate change: The massive CO2 emitter you may not know about*. BBC News. https://www.bbc.com/news/science-environment-46455844

[5]   *Concrete | Definition, Composition, Uses, Types, & Facts*. (2022). Encyclopedia Britannica. https://www.britannica.com/technology/concrete-building-material

[6]   MinuteCement - *Introduction to cement chemistry*. (2014, October 8). YouTube. https://www.youtube.com/watch?v=L4OLBNXMdHk

[7]   Wesselsky, A., & Jensen, O. (2009). *Synthesis of pure Portland cement phases*. Cement and Concrete Research, 39(11), 973–980. https://doi.org/10.1016/j.cemconres.2009.07.013

[8]   Scrivener, K., Füllmann, T., Gallucci, E., Walenta, G., & Bermejo, E. (2004). *Quantitative study of Portland cement hydration by X-ray diffraction/Rietveld analysis and independent methods*. Cement and Concrete Research, 34(9), 1541–1547. https://doi.org/10.1016/j.cemconres.2004.04.014

[9]   Bullard, J. W., Jennings, H. M., Livingston, R. A., Nonat, A., Scherer, G. W., Schweitzer, J. S., Scrivener, K. L., & Thomas, J. J. (2011). *Mechanisms of cement hydration*. Cement and Concrete Research, 41(12), 1208–1223. https://doi.org/10.1016/j.cemconres.2010.09.011

[10] Quennoz, A., & Scrivener, K. L. (2012). *Hydration of C3A–gypsum systems*. Cement and Concrete Research, 42(7), 1032–1041. https://doi.org/10.1016/j.cemconres.2012.04.005

EPFL

[11]   Scrivener, K. (2003). *Calcium aluminate.* Advanced Concrete Technology; Elsevier: Amsterdam, The Netherlands, 1.

[12]   Dilnesa, B., Wieland, E., Lothenbach, B., Dähn, R., & Scrivener, K. (2014). *Fe-containing phases in hydrated cements.* Cement and Concrete Research, 58, 45–55. https://doi.org/10.1016/j.cemconres.2013.12.012

[13]   Bezerra, U. T., Martinelli, A. E., Melo, D. M. A., Melo, M. A. F., & Lima, F. M. (2011). *A correlation between Bogue's equations and Taylor's procedure for the evaluation of crystalline phases in special class Portland oilwell cement clinker.* Cerâmica, 57(341), 122–128. https://doi.org/10.1590/s0366-69132011000100016

[14]   Taylor H.F.W. (1997). *Cement chemistry.* Thomas Telford. www.icevirtuallibrary.com/doi/pdf/10.1680/cc.25929.fm

[15]   Hu, J., Ge, Z., & Wang, K. (2014). *Influence of cement fineness and water-to-cement ratio on mortar early-age heat of hydration and set times.* Construction and Building Materials, 50, 657–663. https://doi.org/10.1016/j.conbuildmat.2013.10.011

[16]   Hyatt, E. P., Cutler, I. B., & Wadsworth, M. E. (1958). *Calcium Carbonate Decomposition in Carbon Dioxide Atmosphere.* Journal of the American Ceramic Society, 41(2), 70–74. https://doi.org/10.1111/j.1151-2916.1958.tb13521.x

[17]   Scrivener, K. L., Lothenbach, B., de Belie, N., Gruyaert, E., Skibsted, J., Snellings, R., & Vollpracht, A. (2015). *TC 238-SCM: hydration and microstructure of concrete with SCMs.* Materials and Structures, 48(4), 835–862. https://doi.org/10.1617/s11527-015-0527-4

[18]   Scrivener, K., Martirena, F., Bishnoi, S., & Maity, S. (2018). *Calcined clay limestone cements (LC3).* Cement and Concrete Research, 114, 49–56. https://doi.org/10.1016/j.cemconres.2017.08.017

[19]   Berodier, E., & Scrivener, K. (2015). *Evolution of pore structure in blended systems.* Cement and Concrete Research, 73, 25–35. https://doi.org/10.1016/j.cemconres.2015.02.025

[20]   Sánchez Berriel, S., Favier, A., Rosa Domínguez, E., Sánchez Machado, I., Heierli, U., Scrivener, K., Martirena Hernández, F., & Habert, G. (2016). *Assessing the environmental and economic potential of Limestone Calcined Clay Cement in Cuba.* Journal of Cleaner Production, 124, 361–369. https://doi.org/10.1016/j.jclepro.2016.02.125

[21]   Scrivener, K. L., John, V. M., & Gartner, E. M. (2018). *Eco-efficient cements: Potential economically viable solutions for a low-CO2 cement-based materials industry*. Cement and Concrete Research, 114, 2–26. https://doi.org/10.1016/j.cemconres.2018.03.015

[22]   Limestone Calcined Clay Cement. (2022). *LC3*. http://www.lc3.ch

[23]   Antoni, M., Rossen, J., Martirena, F., & Scrivener, K. (2012). *Cement substitution by a combination of metakaolin and limestone*. Cement and Concrete Research, 42(12), 1579–1589. https://doi.org/10.1016/j.cemconres.2012.09.006

[24]   Chen, Q., Hills, C., Tyrer, M., Slipper, I., Shen, H., & Brough, A. (2007). *Characterisation of products of tricalcium silicate hydration in the presence of heavy metals*. Journal of Hazardous Materials, 147(3), 817–825. https://doi.org/10.1016/j.jhazmat.2007.01.136

[25]   Ataie, F. F., Juenger, M. C., Taylor-Lange, S. C., & Riding, K. A. (2015). *Comparison of the retarding mechanisms of zinc oxide and sucrose on cement hydration and interactions with supplementary cementitious materials*. Cement and Concrete Research, 72, 128–136. https://doi.org/10.1016/j.cemconres.2015.02.023

[26]   Nonat, A. (2004). *The structure and stoichiometry of C-S-H*. Cement and Concrete Research, 34(9), 1521–1528. https://doi.org/10.1016/j.cemconres.2004.04.035

[27]   Scrivener, K. L., & Nonat, A. (2011). *Hydration of cementitious materials, present and future*. Cement and Concrete Research, 41(7), 651–665. https://doi.org/10.1016/j.cemconres.2011.03.026

[28]   Ouzia, A., & Scrivener, K. (2019). *The needle model: A new model for the main hydration peak of alite*. Cement and Concrete Research, 115, 339–360. https://doi.org/10.1016/j.cemconres.2018.08.005

[29]   Sakalli, Y., & Trettin, R. (2015). *Investigation of C3S hydration by environmental scanning electron microscope*. Journal of Microscopy, 259(1), 53–58. https://doi.org/10.1111/jmi.12247

[30]   Tajuelo Rodriguez, E., Richardson, I. G., Black, L., Boehm-Courjault, E., Nonat, A., & Skibsted, J. (2015). *Composition, silicate anion structure and morphology of calcium silicate hydrates (C-S-H) synthesised by silica-lime reaction and by controlled hydration of tricalcium silicate (C3S)*. Advances in Applied Ceramics, 114(7), 362–371. https://doi.org/10.1179/1743676115y.0000000038

EPFL

[31] Kumar, A., Walder, B. J., Kunhi Mohamed, A., Hofstetter, A., Srinivasan, B., Rossini, A. J., Scrivener, K., Emsley, L., & Bowen, P. (2017). *The Atomic-Level Structure of Cementitious Calcium Silicate Hydrate*. The Journal of Physical Chemistry C, 121(32), 17188–17196. https://doi.org/10.1021/acs.jpcc.7b02439

[32] Harris, M., Simpson, G., Scrivener, K., & Bowen, P. (2022). *A method for the reliable and reproducible precipitation of phase pure high Ca/Si ratio (>1.5) synthetic calcium silicate hydrates (C-S-H)*. Cement and Concrete Research, 151, 106623. https://doi.org/10.1016/j.cemconres.2021.106623

[33] Black, L., Garbev, K., Beuchle, G., Stemmermann, P., & Schild, D. (2006*). X-ray photoelectron spectroscopic investigation of nanocrystalline calcium silicate hydrates synthesised by reactive milling*. Cement and Concrete Research, 36(6), 1023–1031. https://doi.org/10.1016/j.cemconres.2006.03.018

[34] Wedding, P., Odler, I., & Abdul-Maula, S. (1987). *Effect of Chemical Admixtures on Portland Cement Hydration*. Cement, Concrete and Aggregates, 9(1), 38. https://doi.org/10.1520/cca10396j

[35] Odler, I., & Abdul-Maula, S. (1983). *Polymorphism and Hydration of Tricalcium Silicate Doped With ZnO*. Journal of the American Ceramic Society, 66(1), 1–04. https://doi.org/10.1111/j.1151-2916.1983.tb09956.x

[36] Morales, A. (2020). *First Year Candidacy Report*. LMC, EPFL. Personal communication.

[37] Morales, A. (2021). *Second Year Candidacy Report*. LMC, EPFL. Personal communication.

[38] Snellings, R. (2017). Chapter 4: X-ray powder diffraction applied to cement. In Scrivener, K., Snellings, R., & Lothenbach, B.. *A Practical Guide to Microstructural Analysis of Cementitious Materials* (pp.107-176). CRC Press.

[39] Lothenbach, B., Durdzinski, P., De Weerdt. K., (2017). Chapter 5: Thermogravimetric analysis. In Scrivener, K., Snellings, R., & Lothenbach, B.. *A Practical Guide to Microstructural Analysis of Cementitious Materials* (pp.177-212). CRC Press.

[40] Palacios, M., Kazemi-Kamyab, H., Mantellato, S., Bowen, P., (2017). Chapter 10: Laser diffraction and gas adsorption techniques. In Scrivener, K., Snellings, R., & Lothenbach, B.. *A Practical Guide to Microstructural Analysis of Cementitious Materials* (pp.445-484). CRC Press.

EPFL

[41]　T. Allen, (1997). *Particle Size Measurement*, Fifth edition, Chapman and Hall, New York.

[42]　The International Union of Pure and Applied Chemistry (IUPAC). (2022). *IUPAC - electrokinetic potential (E01968)*. IUPAC. https://goldbook.iupac.org/terms/view/E01968

[43]　Malvern Instruments. (2015). *Zeta potential - An introduction in 30 minutes*. Technical Note.

[44]　Barbosa, J. A., Abdelsadig, M. S., Conway, B. R., & Merchant, H. A. (2019). *Using zeta potential to study the ionisation behaviour of polymers employed in modified-release dosage forms and estimating their pKa.* International Journal of Pharmaceutics: X, 1, 100024. https://doi.org/10.1016/j.ijpx.2019.100024

[45]　Scrivener, K., Bazzoni, A., Mota, B., Rossen, J. E., (2017). Chapter 8: Electron microscopy. In Scrivener, K., Snellings, R., & Lothenbach, B.. *A Practical Guide to Microstructural Analysis of Cementitious Materials* (pp.351-418). CRC Press.

[46]　Smith, Y. B. (2018, August 23). *What is Optical Microscopy?* News-Medical.Net. https://www.news-medical.net/life-sciences/What-is-Optical-Microscopy.aspx

[47]　John, E., Epping, J. D., & Stephan, D. (2019). *The influence of the chemical and physical properties of C-S-H seeds on their potential to accelerate cement hydration.* Construction and Building Materials, 228, 116723. https://doi.org/10.1016/j.conbuildmat.2019.116723

[48]　Casar Z. (2022). LMC, EPFL. Personal communication.

[49]　Viallis-Terrisse, H., Nonat, A., & Petit, J. C. (2001). *Zeta-Potential Study of Calcium Silicate Hydrates Interacting with Alkaline Cations*. Journal of Colloid and Interface Science, 244(1), 58–65. https://doi.org/10.1006/jcis.2001.7897

[50]　Yoshida, S., Elakneswaran, Y., & Nawa, T. (2021). *Electrostatic properties of C–S–H and C-A-S-H for predicting calcium and chloride adsorption*. Cement and Concrete Composites, 121, 104109. https://doi.org/10.1016/j.cemconcomp.2021.104109

[51]　Jennings, H. M. (2008). *Refinements to colloid model of C-S-H in cement: CM-II*. Cement and Concrete Research, 38(3), 275–289. https://doi.org/10.1016/j.cemconres.2007.10.006

EPFL

[52] Harris, M. (2022, January 27). *Surface Meeting, Zeta Potential* [PowerPoint slides]. LMC, EPFL. Personal communication.

[53] Barzgar, S., Lothenbach, B., Tarik, M., di Giacomo, A., & Ludwig, C. (2020). *The effect of sodium hydroxide on Al uptake by calcium silicate hydrates (C S H)*. Journal of Colloid and Interface Science, 572, 246–256. https://doi.org/10.1016/j.jcis.2020.03.057

[54] Labbez, C., Pochard, I., Jönsson, B., & Nonat, A. (2011). *C-S-H/solution interface: Experimental and Monte Carlo studies*. Cement and Concrete Research, 41(2), 161–168. https://doi.org/10.1016/j.cemconres.2010.10.002

EPFL

Annexe

The following figures show the XRD diffractograms for "wet" samples of Zn-modified C-S-H with 0.15, 0.2, 0.3 and 0.4 Zn:Si.
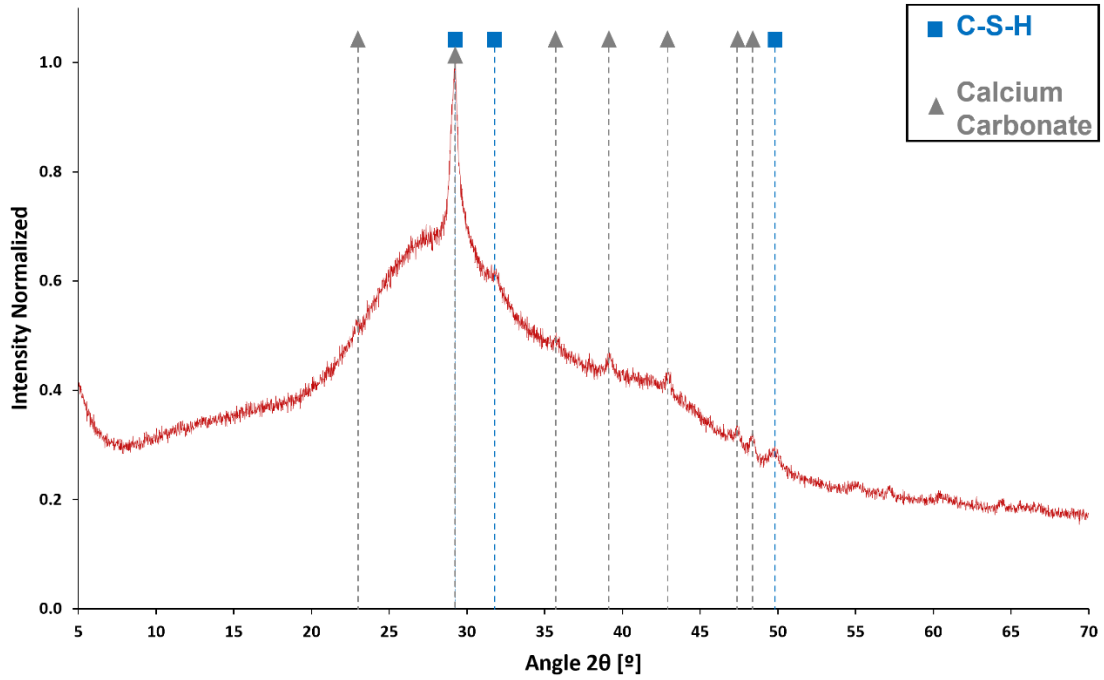

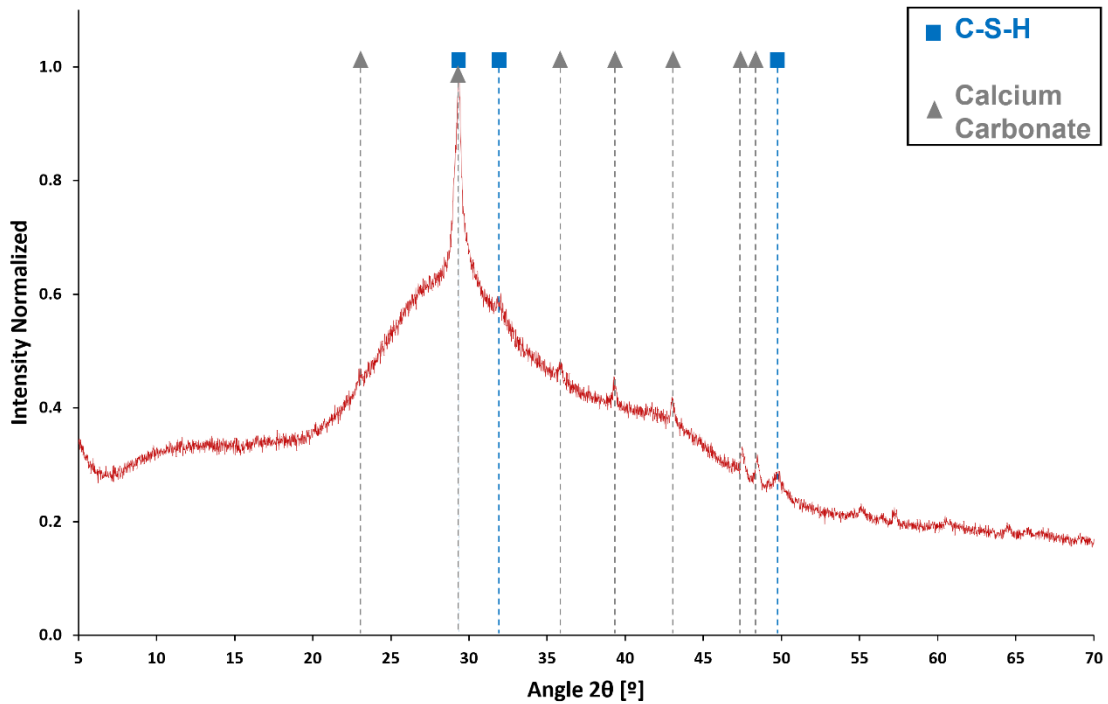*Figure 34: XRD diffractogram of Zn-modified C-S-H with 0.15 Zn:Si ratio.*

Figure 35: XRD diffractogram of Zn-modified C-S-H with 0.2 Zn:Si ratio.
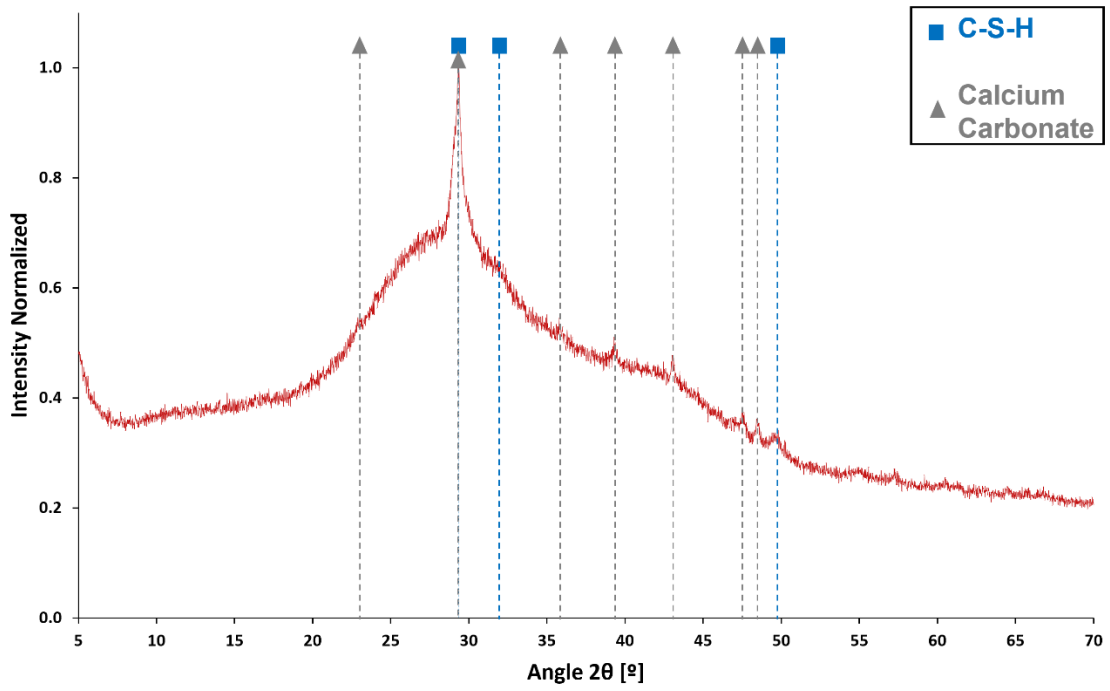
EPFL

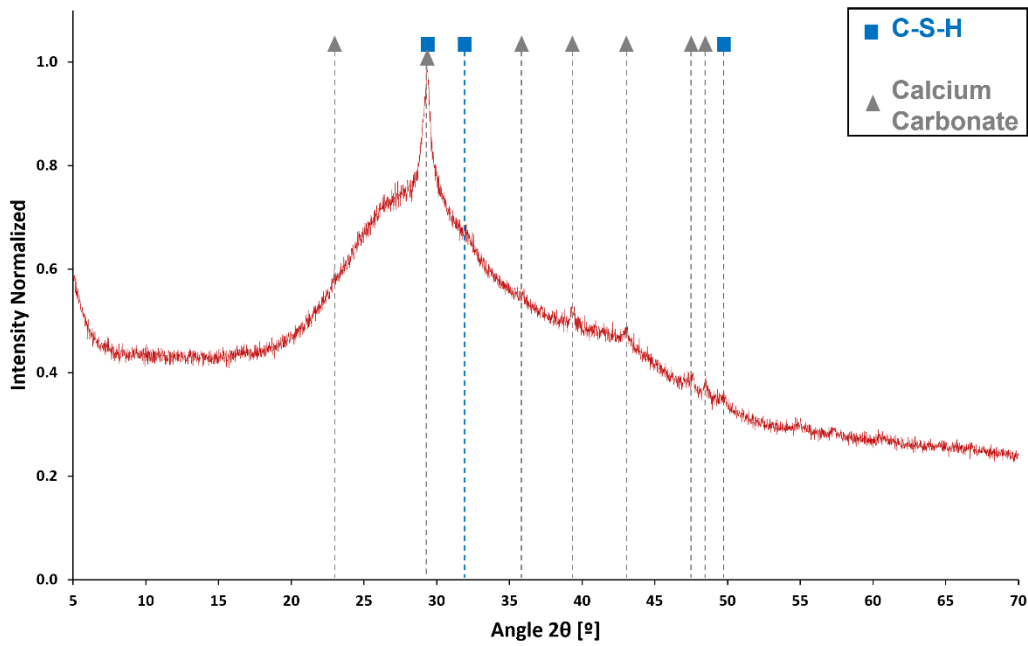*Figure 36: XRD diffractogram of Zn-modified C-S-H with 0.3 Zn:Si ratio.*

Figure 37: XRD diffractogram of Zn-modified C-S-H with 0.4 Zn:Si ratio.

EPFL